# Stereovision Correction Using Modal Analysis

Prather J. Lanier

Thesis submitted to the Faculty of the
Virginia Polytechnic Institute and State University
in partial fulfillment of the requirements for the degree of

Master of Science
in
Mechanical Engineering

Kevin B. Kochersberger, Chair
Alfred L. Wicks
Daniel J. Inman

April 7, 2010
Blacksburg, Virginia

Keywords: Stereo Vision, Modal Analysis, UAV, Gusts Response, Photogrammetry

# Stereovision Correction Using Modal Analysis

Prather J. Lanier

## ABSTRACT

Presently, aerial photography remains a popular method for surveillance of landscapes, and its uses continually grow as it is used to monitor trends in areas such as plant distribution and urban construction. Computer vision and more specifically stereo vision, is one common method of gathering this information. By mounting a stereo vision system on the wings of an unmanned aircraft makes a very useful tool. This technique, however, becomes less accurate as stereo vision baselines become longer, aircraft wingspans are increased, and aircraft wings become increasingly flexible. Ideal stereo vision systems involve stationary cameras with parallel fields of view, but an operational aircraft with a stereo vision system installed, stationary cameras cannot be expected because the aircraft will experience random atmospheric turbulence in the form of gusts that will excite the dominant frequencies of the aircraft.

A method of stereo image rectification has been developed for cases where cameras will be allowed to deflect on the wings of an fixed wing aircraft that is subjected to random excitation. The process begins by developing a dynamic model that estimates the behavior of a flexible stereo vision system and corrects images collected at maximum deflection. Testing of this method was performed on a flexible stereo vision system subjected to resonance excitation where a reduction in stereo vision distance error is shown. Successful demonstration of this ability is then repeated on a flying wing aircraft by the using a modal survey to characterize its behavior. Finally, the flying wing aircraft is subjected to random excitation and a least square fit of the random excitation signal is used to determine points of maximum deflection suitable for stereo image rectification. Using the same techniques for image rectification in resonance excitation, significant reductions in stereo distance errors are shown.

DEDICATION

To Earl Taylor...You will be missed.

# Contents

# List of Figures

# List of Tables

# Chapter 1

# Introduction

In a world where unmanned aerial vehicles (UAV's) are becoming increasingly useful in the reconnaissance and surveillance missions of our armed forces, we are faced with the issue of providing increasingly accurate information. The use of computer vision and more specifically stereo vision, remains a viable and cost effective method of gathering information about unknown terrain which can range from wilderness to urban settings. Information obtained from unmanned aircraft outfitted with such technology has immense potential. This thesis develops a novel technique to correct distance errors that occur in a stereovision system installed on a flexible support; in this case, the wing of an aircraft. These errors are the result of camera motion caused by the bending response of the wing in atmospheric turbulence. By first examining the behavior of a stereovision system placed on a cantilever beam in bending, a method of image correction is established. Once this is successful, a similar method will be applied to a flying wing aircraft whose behavior will be determined

modally.

## 1.1 Project Overview and Motivation

This thesis is written to further research associated with large baseline stereo vision systems installed on flexible beams. The main goal of this project is to prove that through the structural analysis of a flexible beam, such as a wing, corrections can be made to images that have been collected from a stereovision system installed within. The motivation for such research comes from the prior construction of a stereovision boom which was installed on the Yamaha R-max shown in Figure 1.1. After the first flight of this apparatus it became desirable that an investigation be performed to determine the effects of vibration on stereovision images and whether corrections to the collected images could be made.

In the system such as the one pictured pictured in Figure 1.1 , the cameras are mounted on a very stiff carbon fiber tube. If the cameras were placed farther apart, we would need an increasingly stiff beam to prevent camera motion from affecting the accuracy of the stereovision images. Furthermore, this added stiffness incurrs a weight penalty as more structural material is added to provide increased stiffness. It is also important to understand that achieving structural stiffness by adding weight is often impractical in unmanned aircraft design since it reduces the payload capacity of a vehicle where being able to carry additional equipment already comes at a premium. It is for these reasons that the method under examination in this thesis will shift the focus from increasing the structural stiffness of a

Figure 1.1: Stereoboom being flown on autonomous Yamaha R-max.

stereo vision boom to measuring structural deflection. In other words, the system will be allowed to flex, unlike the system pictured in Figure 1.1, and the image improvements will come from adjustments made to the pictures collected and not to the structure itself.

The process by which these stereo images are corrected will require that camera pose infomation be known. This information will be acquired by performing a modal analysis of the aircraft. Results of the modal tests will provide the estimated deflection and rotation angles of cameras installed on the ends of a flexible stereo boom. Combining this information with common principles used in stereo theory will yield greater stereo derived distance accuracies.

# Chapter 2

# Literature Review

## 2.1 History of Aerial Photography

Aerial photography has been, and will continue to be, a widely used method for gathering information about landscapes around the world. Man's fascination with aerial photographs was evident as soon as he was able to take to the air with adequate technologies. The first documented aerial photographs were taken in 1858 when French photographer and balloonist Gaspard Felix Tournachon used his tethered ballon to take aerial images of Paris so they could be used as a reference for artistic renderings of the city. Realizing the unique nature of what he had just accomplished, Tournachon, also known as Nadar, applied for a patent for what is now known as an aerial survey. In this patent, he describes mapping a landscape with a series of overlapping photographs [1]. It would not be long before word of this amazing

feat would reach the Americas and aeronauts would take to the skies in attempts to mimic Nadar's technique.

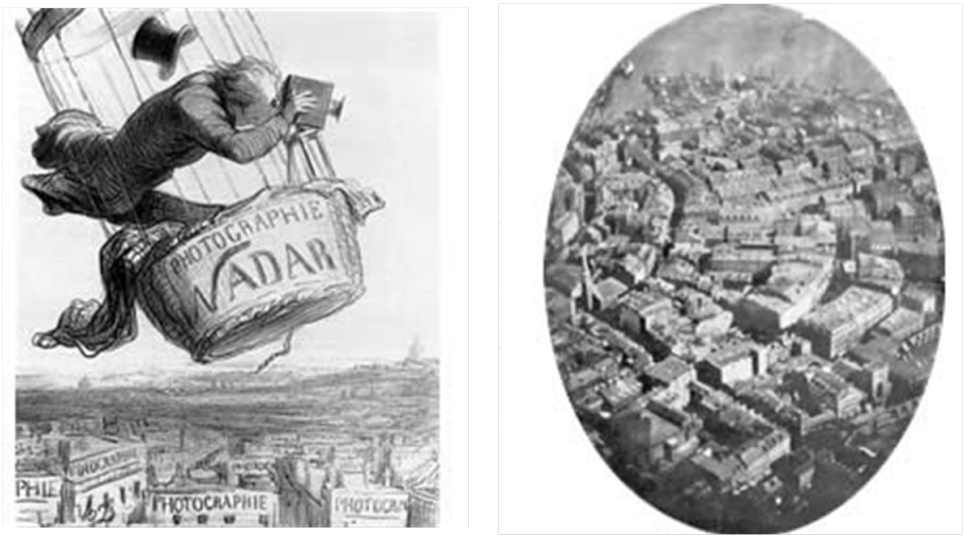


Figure 2.1: Drawing of French photographer Gaspard Felix Tournachon taking the first aerial images (Left). First aerial picture of the city of Boston (Right)[1].

In the years to follow, even more creative methods were used in the collection of aerial photographs, such as attaching cameras to kites, rockets, and even pigeons. Eventually, in 1909, Wilbur Wright and L.P. Bonvillan produced aerial images from an airplane as they flew over the city of Le Mans, France, using a motion picture camera. Successive flight attempts by the Wright brothers and many others proved that the airplane was the best platform for the collection of aerial images. By the end of World War I, the use of airplanes to collect aerial photographs had become a standard practice as planes were used for reconnaissance missions.

As military use drove the need for more than just 2-D spatial information to be collected from images, more complex image evaluation methods developed. Photogrammetry, or the

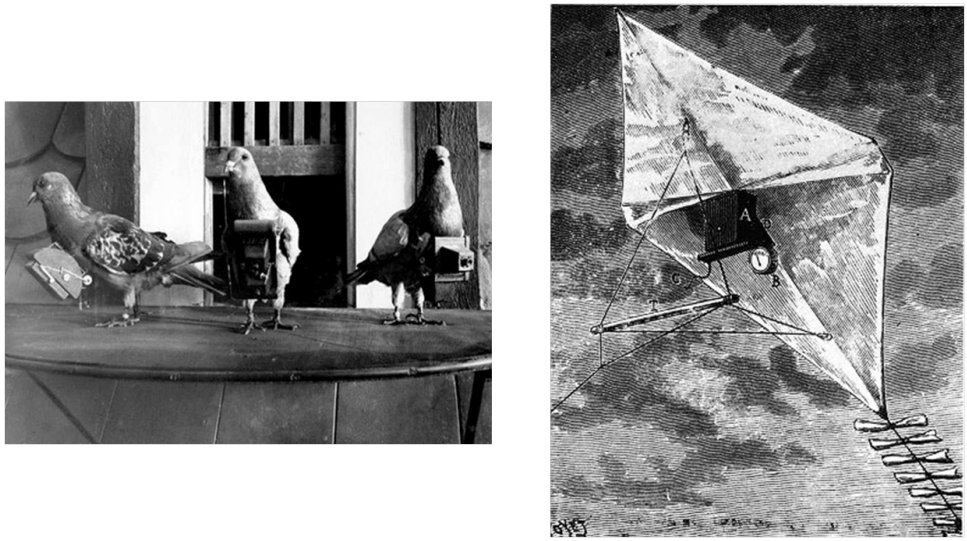

Figure 2.2: Balloons were not the only vehicles used for aerial photography. The image above shows examples alternative vessels used to gather aerial images[1].

precise measurement of the earth's surface in three dimensions based on aerial photographs, was heavily studied [1]. One technique involved taking overlapping images from a single camera over a known surface area from a known altitude. By providing an image overlap of at least 30 %, precise maps could be created with errors of less than 1 %. Use of this technique had its drawbacks, as it was only accurate when photographs were taken over flat surfaces. Another method allowed three-dimensional information to be collected over irregular surfaces. This method, which enabled scientists to extract depth information from two views of a selected landscape, is called stereo vision.

## 2.2 Stereovision Overview

The concept of deriving depth information from two views of a scene has existed since the 1830's when the stereoscope was invented by Sir Charles Wheatstone [2]. This device was created to view stereographs, two images of a scene which vary in their horizontal placement. Each eye is presented with a single image and as the brain processes the two, depth information is created.

Figure 2.3: Example of stereovision system [3].

The process is similar in a system used on an airplane since stereo vision is accomplished by using two or more cameras to capture images of the same three-dimensional scene from opposing views. As a result of the cameras being in different positions, differences in the appearance of corresponding points between simultaneously collected images can be observed. This phenomenon, known as stereo disparity, can be used to collect three-dimensional information from multiple two-dimensional images [2]. One common stereo imaging system is shown in Figure 2.3. Notice that the cameras shown are horizontally aligned and separated by a baseline distance.

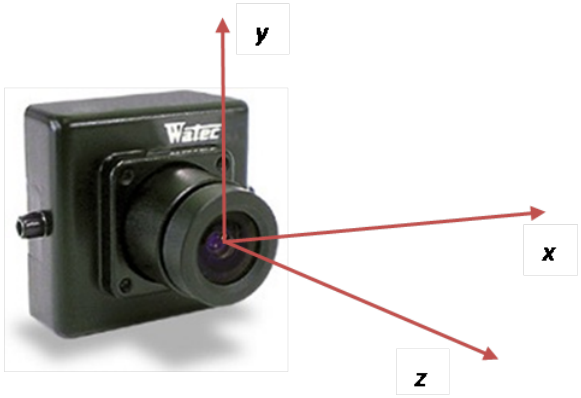


Figure 2.4: Camera-centered coordinate system. This picture shows a Watec 660D G3.8 mono board camera, which is one of the models used for this project.

Consideration, in this thesis, is given to cameras separated by a relatively large baseline distance. Additionally, these cameras have been placed on a structural support that will be allowed to flex when subjected to vibration. The main objective is to study the rotation of the cameras in opposite directions about their respective y-axes. Vibration will tend to cause the cameras to rotate toward and away from each other repeatedly.To reduce the effects of motion blur caused by these vibrations, images will be collected at the wing's maximum deflection, which corresponds to minimum camera motion. The disparity values for corresponding points will be smaller or larger, depending on whether the wing is bending up and down, than for the calibrated (stationary) system; this results in the estimated distance being closer or farther than the true values. For example, at maximum deflection during divergence, the disparity values would be larger and the estimated distance values would be smaller than the calibrated values. Tracking the points of maximum deflection that correspond to minimum camera motion presents the experimenter with a unique challenge. One method to solve this problem involves exciting a structure, such as an airplane, with

a known signal and measuring its response [4]. This method will be introduced in the next section.

## 2.3 Modal Characterization of Aircraft

Modal testing or analysis presently employs the use of modern data acqusition systems in combination with force transducers and accelerometers to measure these responses. Ground vibration testing (GVT) is a popular method of modal analysis that is used in large aircraft. A GVT is typically performed late in the manufacturing process of large aircraft to test how well the actual aircraft correlates with analytical models created to predict its performance.

Papers written by Kehoe, Peeters, and Pickrel examine the methods used in ground vibration testing to gather structural responses in effort to identify critical modes, some of which may cause aircraft flutter. Both execute similar tests, using random excitations to identify frequencies of interest by examination of the frequency response functions (FRF's). They then refine their experiment by using frequency dwells or sweeps to examine the aircraft's response at selected frequencies that encompass realistic operating conditions [6], [7], [8]. Pickrel also explains what he defines as a modal pretest, or a methodology behind modal testing for structures. He identifies several topics that must be considered prior to testing, such as valid frequency ranges, target modes, sensor locations, and shaker-stinger attachment effects to improve the modal tests that aim to validate analytical models [9].

Although the methods of ground vibration testing previously mentioned are in refer-

ence to tests performed on large aircraft, the same techniques apply to the tests that will ultimately be performed on small unmanned aircraft, many times lighter and much more fragile than the aircraft considered by Kehoe, Peeters, and Pickrel. Woehrle [10], performs modal testing on a small unmanned aircraft named Pathfinder using techniques identical to those used in the examination of large aircraft. However, special consideration is given to the method Woehrle uses to create the free-free boundary conditions needed to test this smaller aircraft. Bungee cords are employed to achieve the free-free boundary conditions appropriate for the test[10].

## 2.4 Aircraft Gust Response

Gusts are the predominant excitation source that induces aircraft modal vibration. Gusts are considered to be random in nature and have the ability to affect a variety of aspects of to aircraft operation [11],[12]. An understanding of gust response plays a vital role in the design of aircraft surfaces, and the evaluation of this phenomenon is a considerable random dynamic problem. Aerial vehicles can experience gusts from any direction, but for simplicity Hoblit [13] expresses the fundamentals of gusts using horizontal and vertical components. When a gust acting upon an aircraft is continuous, it is defined as turbulence. When this profile is plotted in space it takes on an irregular form as illustrated in Figure 2.5.

For the purposes of this research, it will be necessary to map the predominate bending modes in a flying wing by using random excitations intended to simulate a "gusting"

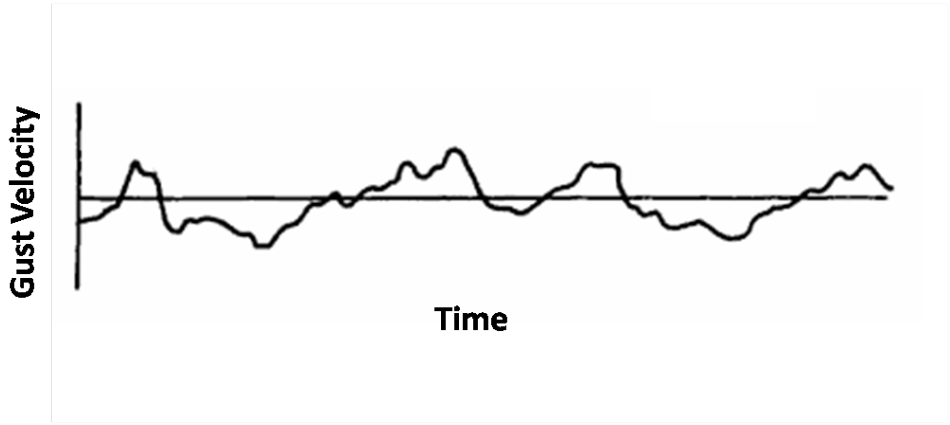


Figure 2.5: Example of a Gust Profile (Reprinted with permission of the American Institute of Aeronautics and Astronautics)[13].

condition through a modal approach. For slender beam systems such as aircraft wings, gust conditions are expected to excite predominately the first mode wing bending. This concept is discussed by Eslimy-Isfahany and Banerjee [14]. Additionally, it is shown that the second bending mode frequencies for beams are approximately five times higher than the first bending mode frequencies. Combination of this information with Balakrishnan [15], who showned that turbulence energy for subsonic flight is concentrated at very low frequencies, suggests the first bending mode will dominate the response of a wing in atmospheric turbulence. Finally, Bennett and Yntema [16] derive a method of calculating wing excitation from turbulence that considers plunging rigid body motion and the first wing bending mode, further reinforcing the concept that only the first flexible bending mode is typically excited in turbulence.

Utilizing the information explored in this background section in combination with common engineering principles, a dynamic model of a wing-mounted stereo vision system

can be formulated. Formation of a realistic dynamic model is paramount to the sucess of this research. A proper model will provide the experimenter with the attributes of the stereo vision system that will allow for stereo image distance correction. The following section describes this process.

# Chapter 3

# Development of a Flexible Beam-Camera System Model

Developing a proper dynamic model of a flexible stereo vision system is essential to predicting the motion of a wing mounted camera. As a minimum requirement, a proper model will provide the experimenter with three specific attributes. The first of these is the natural frequencies associated with each mode, and, more specifically, low frequency bending modes since they will dominate the free response of the system. Next, the model should enable the experimenter to estimate the beam deflection at every point along its length to determine the stereo camera's deflection. Finally, the model should provide the experimenter with an accurate estimate of the slope of the beam, as this is what will make stereo distance correction possible.

## 3.1 Preliminary Model Development

To begin to develop a model by which we can approximate the modal frequencies and shapes of the stereo vision boom, it is necessary to make several assumptions. The first of these is to assume that the cameras are centrally supported. For example, the cameras could be placed along the wings of an airplane with the fuselage acting as a mounting point. Next, since the cameras are centrally supported, it can be assumed that this central support creates a fixed end condition on either side with the beam on which the cameras are attached. The cameras, which are attached to the ends of this beam, will be treated as tip masses. Figure 3.1 is a simple drawing the aforementioned system.

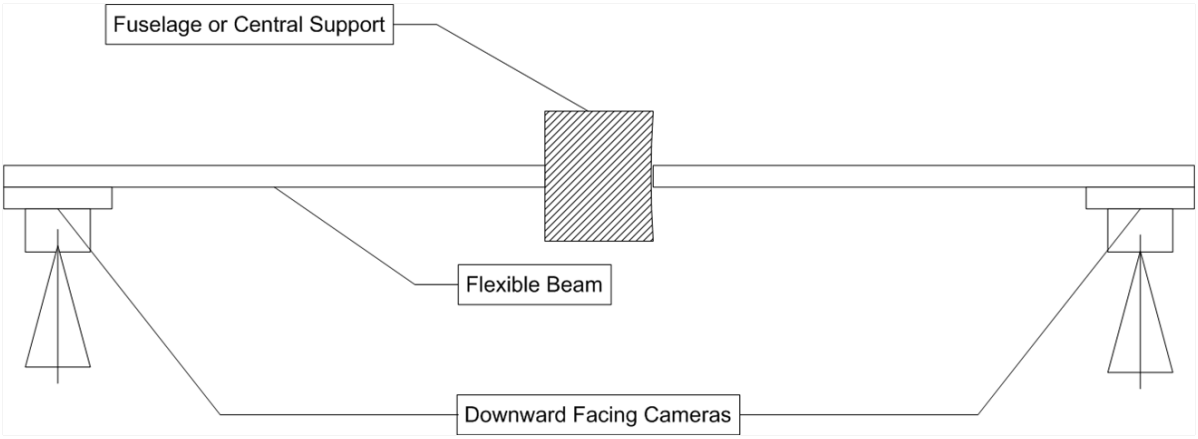


Figure 3.1: Represenation of Beam-Camera system. Each beam is fixed at the central support and the cameras will be treated as tip masses.

Recognizing that there is symmetry in the stereo vision system that will be created, the system may be simplified to estimate its basic behavior. By reducing this system to its most basic parts, as shown in Figure 3.2, a beam with spring force of k which is based on its material properties (elastic modulus E, moment of inertia I,length L), and a tip mass with

a mass of m, it is possible to determine the approximate first natural frequency of the wing in transverse vibration using equation 3.1.

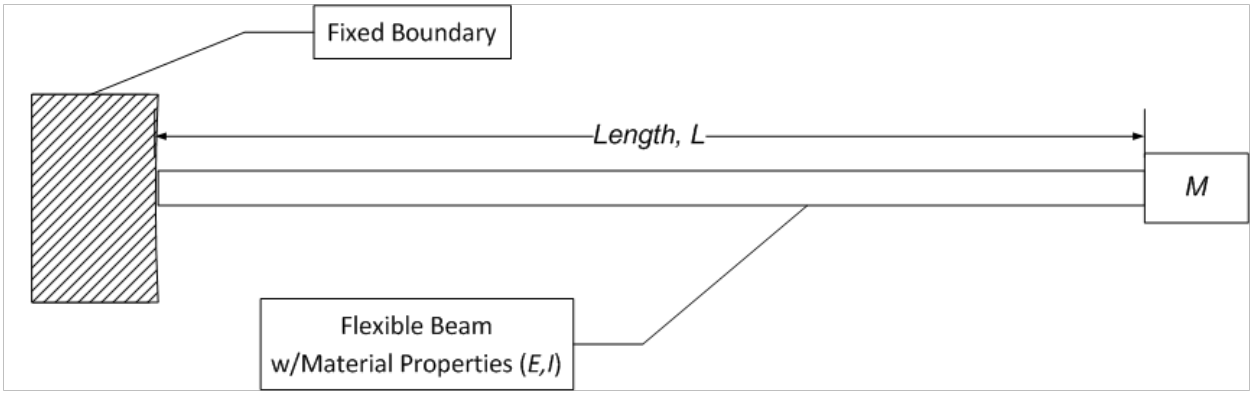


Figure 3.2: Reduction of Stereoboom to it most basic components. Symmetry allows for an approximate system behavior to be determined by the examination of only one side.

$$\omega_n = \sqrt{\frac{k}{m}} = \sqrt{\frac{3EI}{ml^3}} \tag{3.1}$$

While this model is far from true wing behavior, since it can be shown that actual aircraft will exhibit antisymmetric modes that can not be represented in a symmetric model, it is representative of the type of motion that will be excited by gusts on a small aicraft. A symmetric response is expected due since the dimensions of the gust relative to the size of the aircraft will be much larger. The first bending mode, as mentioned in section 2.4, will dominate the free response of a long slender beam. This simplified estimation, using a point mass and no inertia, of the first bending mode will be used in the preliminary design of a flexible stereo vision system created for this experiment, shown in figure 3.3.

The bolts in the center of this flexible stereo vision system will be used as attachment

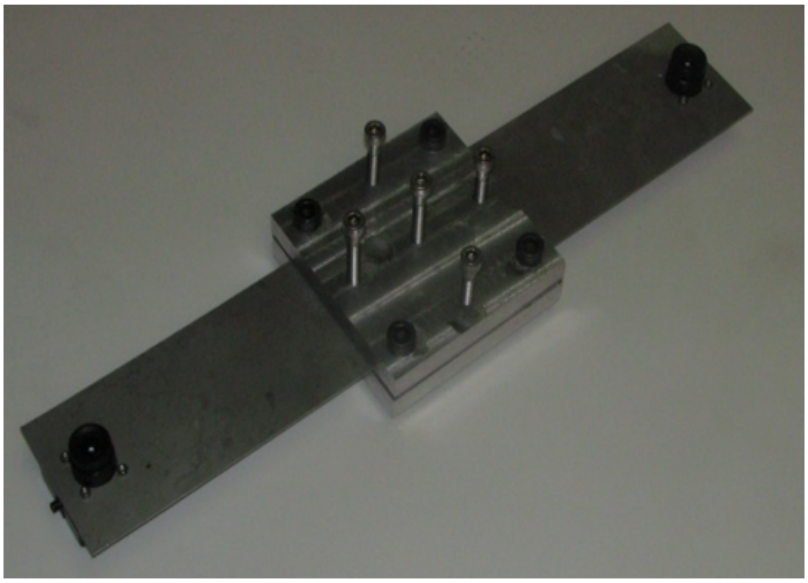

Figure 3.3: Experimental Flexible Stereo Boom.

points to excite this structure. Using this technique, when the structure is excited at resonance, the center displacement will be nearly zero and each camera will act as if it were mounted on an individual cantilever beam.

## 3.2 Dynamic Model for Stereo Vision Distance Correction

A more correct analytical model of the beam-camera system is derived using an Euler-Bernoulli beam model. More complex wing shapes will require FEA to obtain an analytical deflection shape. Development of this model is as follows:

The governing equation of vibration for the Euler-Bernoulli beam is[17].

$$\frac{\delta^2 Y(x,t)}{\delta t^2} + c^2 \frac{\delta^4 Y(x,t)}{\delta x^4} = 0 \; where \; c = \sqrt{\frac{EI}{\rho A}}. \tag{3.2}$$

The solution of the spatial equation has the form $Ae^{\sigma x}$, and the general solution of the spatial equation is

$$Y_n(x) = c_1 \sin \beta_n x + c_2 \cos \beta_n x + c_3 \sinh \beta_n x + c_4 \cosh \beta_n x. \tag{3.3}$$

Where $c_n$ values are the modal constants that will be determined by the boundary conditions of a cantilever beam with a tip mass, which for the fixed end are

$$Y = 0 \qquad \frac{\delta Y}{\delta x} = 0 \tag{3.4}$$

and for the free end,

$$EI \frac{\delta^2 Y}{\delta x^2} = 0 \qquad EI \left( \frac{\delta}{\delta x} \right) \frac{\delta^2 Y}{\delta x^2} = -m\ddot{\omega}. \tag{3.5}$$

These boundary conditions assume that the tip mass (camera) has a very small rotary inertia compared to the beam. Differentiating equation 3.3 and applying the appropriate boundary conditions results in

$$\begin{bmatrix} 0 & 1 & 0 & 1 \\ 1 & 0 & 1 & 0 \\ -\sin\beta l & -\cos\beta l & \sinh\beta l & \cosh\beta l \\ A & B & C & D \end{bmatrix} \begin{bmatrix} c_1 \\ c_2 \\ c_3 \\ c_4 \end{bmatrix} = \begin{bmatrix} 0 \\ 0 \\ 0 \\ 0 \end{bmatrix} \tag{3.6}$$

where A,B,C, and D equal,

$$A = -EI\beta^3 \cos\beta l + m\ddot{\omega}^2 \sin\beta l \tag{3.7}$$

$$B = -EI\beta^3 \sin\beta l + m\ddot{\omega}^2 \cos\beta l \tag{3.8}$$

$$C = -EI\beta^3 \cosh\beta l + m\ddot{\omega}^2 \sinh\beta l \tag{3.9}$$

$$D = -EI\beta^3 \sinh\beta l + m\ddot{\omega}^2 \cosh\beta l \tag{3.10}$$

For a non-zero solution, the leading matrix determinant is set to zero, which provides the roots of the system. With the aid of the physical properties of the beam shown in 3.2, these roots can be used to determine the natural frequencies of our test camera boom. Using this

approach, the fundamental bending frequencies of the system are found. The results are listed in table 3.2.

Table 3.1: Physical properties of beam.

| Beam Properties | |
|---|---|
| Young's Modulus,(E) | $70 \times 10^9$ GPa |
| Density,($\rho$) | 2700 $\frac{kg}{m^3}$ |
| Inertia,(I) | $4.225 \times 10^{-}12\ m^4$ |
| Cross Sectional Area,(A) | $5.07 \times 10^{-}5\ m^2$ |
| Mass of Tip Mass,(m) | .035 Kg |
| Length of beam,(l) | .1115m |

Table 3.2: Physical properties of beam.

| Mode | $\beta l$ Values | Frequency (Rad/s) | Frequency (Hz) |
|---|---|---|---|
| 1 | 1.047 | 126.3 | 20.1 |
| 2 | 3.974 | 1865.8 | 296.9 |
| 3 | 7.098 | 5952.3 | 947.3 |

After obtaining the natural frequencies of our stereo beam system, the modes of vibration are determined by substituting the $\beta l$ values. Figure 3.4 shows the first mode shape (displacement) along with the derivative of this shape to obtain the modal slopes. It will be the slope plot that is used to correct the camera pose so that correct distances are obtained from the stereo image pair.

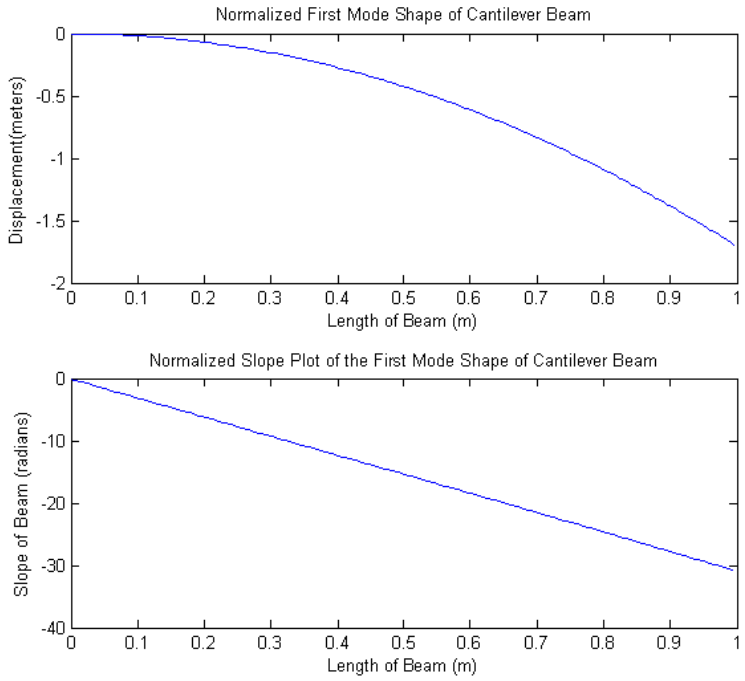


Figure 3.4: Normalized First Mode Shape of Stereo boom (Top). Normalized Slope along the length of stereo boom (Bottom).

## 3.3 Mathematical Method for Stereo Image Correction

Lanier and Short [18] present stereovision theory that can be used to correct the three dimensional information collected from cameras whose lenses may be bending toward or away from each other. Stereo ranging is illustrated with the simple arrangement that is shown in figure 3.5. In this ideal system, the optical axes of the two cameras are perfectly parallel, both image planes are coplanar, and no lens distortion is present. Scene point P projects onto both image planes, and we would like to recover its 3-D coordinates, or the distance Z (also called the range or depth).We can use the following equation:

$$Z = \frac{Bf}{d} \tag{3.11}$$

In this equation, f is the focal length, B is the baseline, and d is the disparity between two corresponding points, which is given by $d = x_l - x_r$. (In the figure, the value for $x_l$ is negative because it is on the left of the optical axis.) Although stereo ranging is simple in principle, the identification of point correspondences between the two images is a diffcult problem.

In an actual stereo system, the optical axes are not perfectly parallel. A calibration procedure is used to determine the relative 3-D orientation between the two cameras, as well as intrinsic parameters such as the focal lengths and image center locations. With this information it is possible to rectify the two images with 2-D transformations that cause

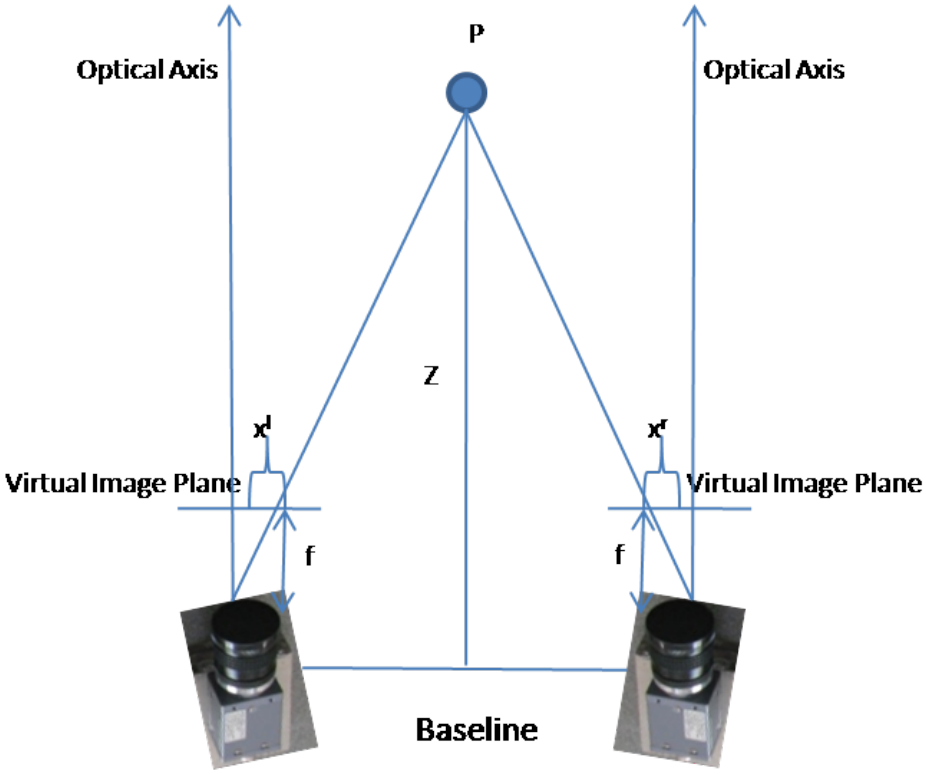


Figure 3.5: Simple geometry for stereo ranging. The usual goal is to find the range Z from the cameras to a point P in the scene.

all corresponding points to be aligned horizontally. Rectification causes the images to resemble the ideal case shown in figure 3.5, and it increases the efficiency of the search for corresponding points.

A rotation matrix can describe the orientation of the left camera with respect to the right, using the camera-centered coordinate system shown in figure 2.4 . The origin is located at the point of projection and the z axis coincides with the optical axis. The x and y axes are parallel to the image plane. Rotation about the x, y, and z axes will be represented as $\Theta_x$(pitch), $\Theta_y$(yaw), and $\Theta_r$ roll of the camera, respectively.

The composite rotation vector RV for one camera can be expressed as the row vector:

$$RV = \begin{bmatrix} \Theta_x & \Theta_y & \Theta_z \end{bmatrix} \tag{3.12}$$

If RV represents a fixed axis through the origin, then the angle of rotation about this axis is given by the vector norm

$$\theta = \left\| RV \right\|, \tag{3.13}$$

and the corresponding unit vector is

$$\Omega = \frac{RV}{\theta} \tag{3.14}$$

with components $\Omega$=[$\Omega_x$ $\Omega_y$ $\Omega_z$ ]. If we now define the antisymmetric matrix

$$\Omega_\nu = \begin{bmatrix} 0 & -\Omega_z & \Omega_y \\ \Omega_z & 0 & -\Omega_x \\ -\Omega_y & \Omega_x & 0 \end{bmatrix}, \tag{3.15}$$

then the rotation matrix is given by

$$R = I + \Omega_v \sin\theta + \Omega_v \Omega_v^T (1 - \cos\theta), \tag{3.16}$$

where I is the 3×3 identity matrix. This is known as Rodrigues' rotation formula [18], and it can be rewritten as

$$R = \begin{bmatrix} \cos\theta + \Omega_x^2(1-\cos\theta) & -\Omega_z \sin\theta + \Omega_x\Omega y(1-\cos\theta) & \Omega_y \sin\theta + \Omega_x\Omega z(1-\cos\theta) \\ \Omega_z \sin\theta + \Omega_x\Omega y(1-\cos\theta) & \cos\theta + \Omega_y^2(1-\cos\theta) & -\Omega_x \sin\theta + \Omega_y\Omega z(1-\cos\theta) \\ -\Omega_y \sin\theta + \Omega_x\Omega z(1-\cos\theta) & \Omega_x \sin\theta + \Omega_y\Omega z(1-\cos\theta) & \cos\theta + \Omega_z^2(1-\cos\theta) \end{bmatrix}, \tag{3.17}$$

For both cameras, the combined rotation matrix is

$$R = R_r R_l^T \tag{3.18}$$

where $R_r$ and $R_l$ are the rotation matrices for the right and left cameras, respectively.

For stereo imaging systems in general, it is assumed that cameras must remain stationary relative to one another. Once calibrated, any change in this position can affect the disparity values of points that have been imaged, this will in turn, reduce the accuracy of any distance measurements made by the stereo ranging system. It is expected that the introduction of vibration will further distort the accuracy of the distance measurements that result from stereo ranging. Vibrations may also introduce motion blur into the images, and this will affect the ability to localize feature points that may be present in stereo images, causing a greater reduction in ranging accuracy.

# Chapter 4

# Test Results of the Flexible Beam-Camera System

Before attempting to build and integrate a stereo vision system onto a flexible wing, the system described in section 3.2 and shown in figure 4.1 will be tested. Utilizing the preliminary design assumptions in section 3.1, the cantilever beam system was designed from aluminum to have a first bending frequency of approximately 20 Hz. Although it may be considered bad practice to design a beam which is to be part of a stereo vision system to be flimsy and have such a low natural frequency, this inherent flexibility is given to the system so that the modal behavior of the system baseline must be characterized to achieve accurate distance measurements from the collected stereo images. Additionally, the low frequency first mode which is present in this system was necessary for the data acquisition system to synchronize camera images with measured accelerations since the cameras used in this preliminary trial

have a maximum frame rate of 30 fps.

## 4.1 Experimental Setup of a Stereo Vision System Subject to Harmonic Vibration

The objective of this test is to prove that camera rotation at maximum modal displacement can be accounted for and used to obtain accurate stereo distance measurements. The maximum displacement of the system is used because this corresponds to a zero velocity of the camera which, in turn, minimizes image blur. The stereo system was built using two Watec 660D cameras, networked with an Axis 241Q Video Server, shown in Figure 4.1 and described in Table 4.1. The cameras were mounted on a beam at a baseline of 10 inches, which was placed on a 50 lb. shaker. The cameras were connected to the video server through two coax video cables and powered at 9 volts through a bench top power supply.

Figure 4.1: Stereo System with two Watec 660D cameras and Axis 241Q Video Server.

The data acquisition system was a Spectral Dynamics model 20-24 digital signal processing (DSP) unit running the SigLab analysis software. Figure 4.2 shows the test compo-

Table 4.1: Camera Specifications for Left and Right Cameras.

| Watec 660D G3.8 Mono Board | |
|---|---|
| Sensor Type | $\frac{1}{4}$" interline transfer CCD |
| Unit Cell Size (physical size on sensor) | 7.15 $\mu$m $\times$ 5.55 $\mu$m |
| Resolution | 704 $\times$ 480 |
| Minimum Illumination | 0.06lx. |
| Focal Length | 3.8 mm |

Table 4.2: Video Encoder Specifications for stereo system.

| AXIS 241Q Video Server | |
|---|---|
| Connection Type | Network Cameras |
| Resolution | Transmits simultaneous streams up to 704 $\times$ 576 |
| Video Frame Rate | Up to 30 fps |
| Number of Channels | 4 |
| Video Format | Motion JPEG and MPEG-4 |

nents.

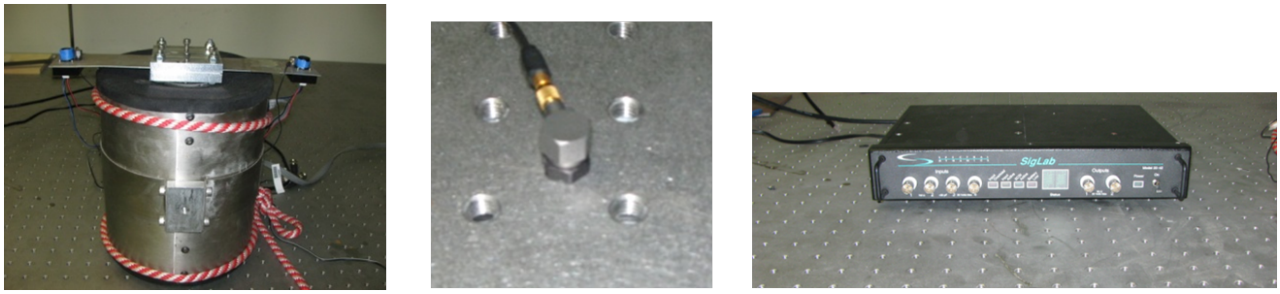


Figure 4.2: Shaker is a Vibration System Model VG10054. Accel is a PCB 35C65 and the analyzer is a Spectral Dynamics 20-24.

The three-Dimensional scene that was analyzed was a set of objects placed on the ceiling above the shaker, on which the stereo system was mounted. This scene is shown in Figure 4.3; newspaper was used as a backdrop to provide a textured background for correlation purposes in the stereo matching routine.

Figure 4.3: View of scene used for measuring distances with stereo system.

Using the SigLab virtual network analyzer function, a continuous sinusoidal input signal was used to excite the stereo vision system at its first fundamental frequency of 20 Hz. Acceleration data was then sampled at a rate of 512 Hz for 20 second periods. These acceleration values can then be converted into beam displacement using the following relationship

$$y(t)_{disp} = \frac{\ddot{y}(t)}{\omega^2} \tag{4.1}$$

where ÿ is the acceleration seen by the accelerometer and $\omega$ is the frequency in radians per second. Figure 4.4 shows the results of one such sample run.

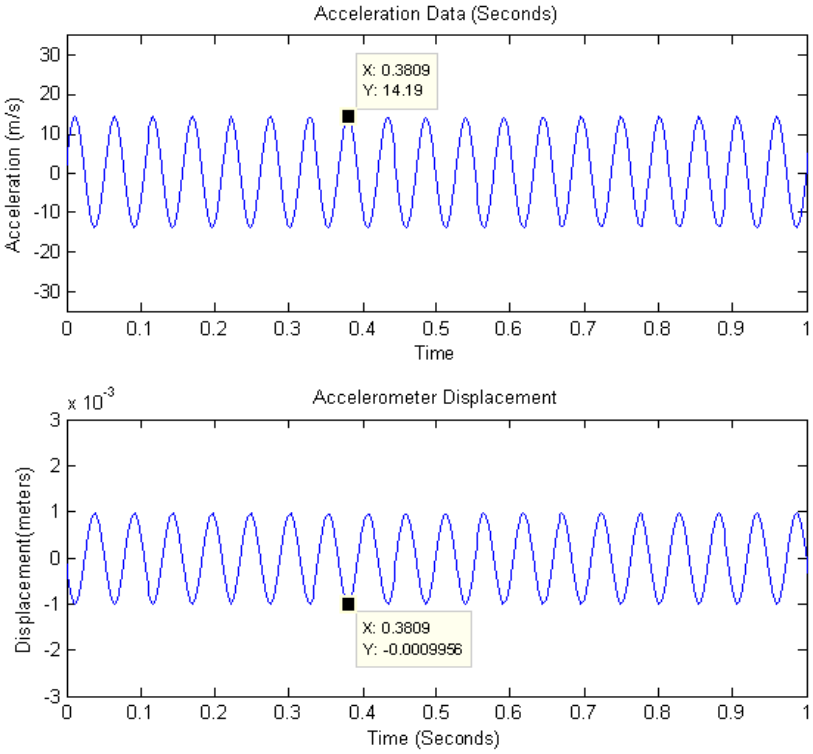


Figure 4.4: Accelerometer Data in m/s (Top). Accelerometer Displacement (Bottom).

## 4.2 Results of a Stereo Vision System Subject to Harmonic Vibration

Figure 4.4 shows a maximum displacement of about 0.995 mm at the location of our accelerometer at an input of 0.015 volts rms. Figure 4.5 displays a plot of our calculated mode shape from equation 3.6 which can be used to determine camera displacement/rotation based on the locations of the accelerometer and the camera. The accelerometer is located at a distance of 87 mm from the fixed end of our stereo vision boom and the camera is located at 97 mm. Using the accelerometer values and the scaled mode shape, the camera displacement

can be obtained.

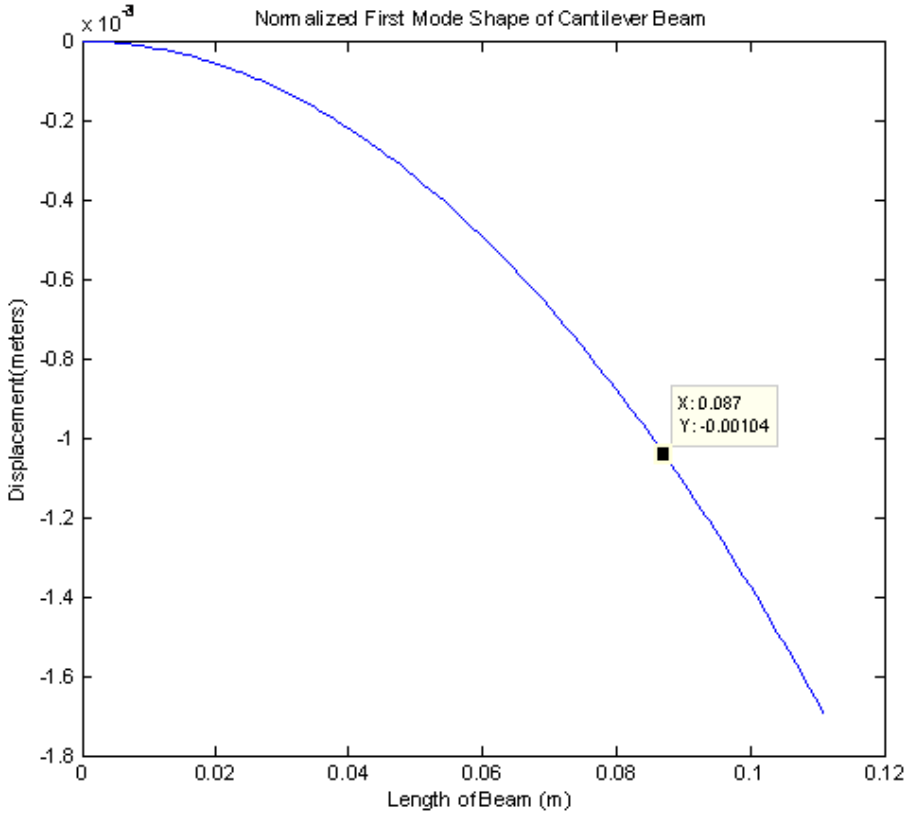


Figure 4.5: Scaled mode shape plot based on measured acceleration at 87 mm.

Additionally, the first mode beam slope, $\frac{\delta Y}{\delta x}$, can be extracted from the mode shape and used to obtain camera rotation angles, and will be used for the camera corrections. In the experimental case, the measured accelerations were used to determine a peak camera rotation angle of 0.0265 radians, shown in Figure 4.6.

Before the experiment was conducted, a set of images were taken while the cameras were motionless to compare the corrected results to the ideal results from the system. The disparity map for this scenario is shown in figure 4.7. This figure shows the relative distance of the objects from the camera. Closer objects are represented as lighter intensities and

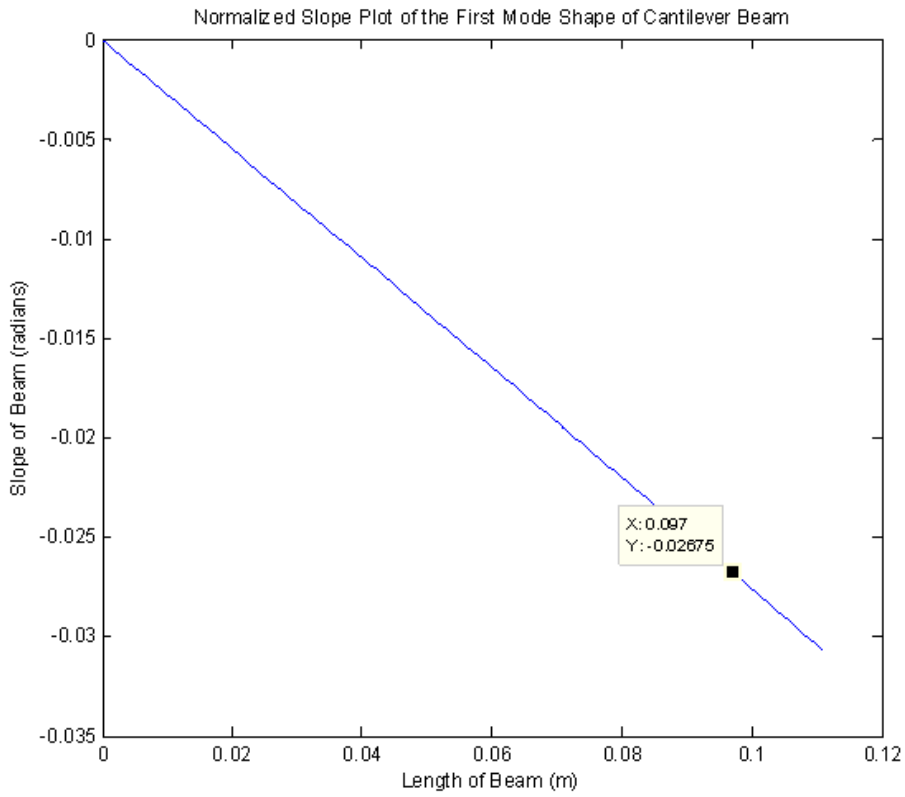


Figure 4.6: Scaled beam slope plot based on distance to center of camera lens at 97 mm.

objects farther away are shown as darker intensities. Table 4.2 shows the results of distance calculations before (top two rows) the shaker is turned on, and after (bottom two rows) the shaker is turned on where images are obtained at the peak acceleration (peak displacement and rotation). Note that distance errors of 19 %represent the maximum error in the oscillatory cycle for an uncorrected set of images, but they also represent the highest quality images because the cameras are momentarily motionless at the peaks of the cycle.

By placing accelerometers on or near the cameras, measured vibration can be used to calculate the deflection angle of the cameras which in turn is used to correct the images using the Rodrigues Rotation Matrix described in section 3.3.

Table 4.3: Results from stereo matching: static (top) and dynamic (bottom). Measurements are distances to the real world points.

| Pixel | Measured | Actual | Percent Error |
|---|---|---|---|
| {263,345} White | 1344.382 mm | 1371.6 mm | 1.98% |
| {222,367} Black | 1163.814 mm | 1168.4 mm | 0.39% |
| Pixel | Measured | Actual | Percent Error |
| {274,345} White | 1109.814 mm | 1371.6 mm | 19.08% |
| {220,341} White | 954.366 mm | 1168.4 mm | 18.31% |

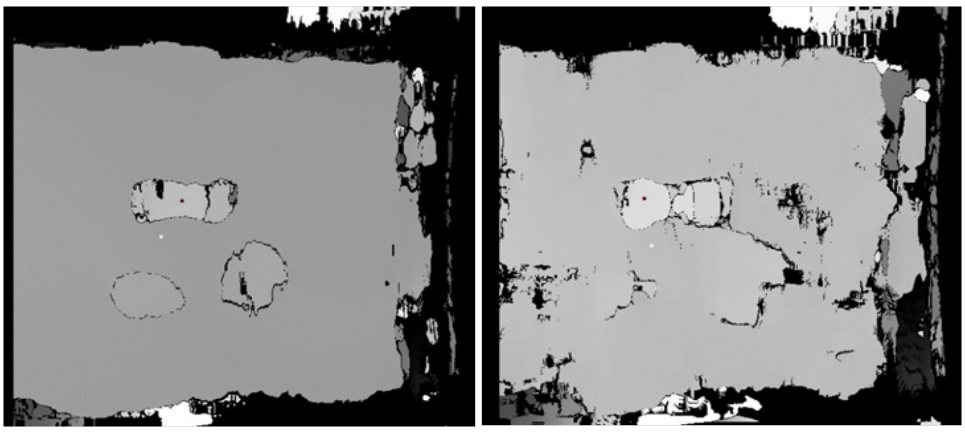

Figure 4.7: Disparity map from correlation without vibration (left) and with vibration (right).

## 4.3 Results of Camera Corrections

In the experiment, the camera angle at peak motion was calculated to be 0.0261 rad, resulting in a $\Theta_y$ of 0.0522 rad which is used in equation 3.12 to obtain the corrected camera pose. The disparity map in figure 4.8 and the calculated error in Table 4.3 show the improvements in calculating depth using the angle calculated from the accelerometer data.

Comparing the results of Table 4.3 to Table 4.2, we see a significant improvement in distance measurements when the angle corrections are applied to the stereo rectification. The error in measured distance dropped 14.5 %for the black marker and 11.94 %for the white

Table 4.4: Error in distance measurement using camera corrections.

| Pixel | Measured | Actual | Percent Error |
|---|---|---|---|
| {265,334} White | 1309.125 mm | 1371.6 mm | 4.55% |
| {230,322} Black | 1093.952 mm | 1168.4 mm | 6.37% |

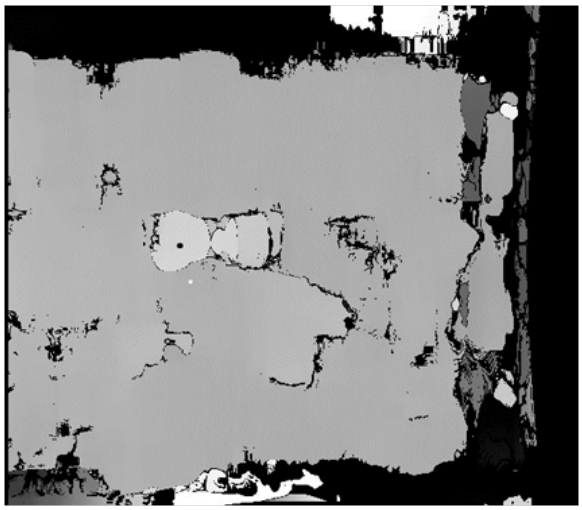

Figure 4.8: Disparity map from correlation without vibration and correction angle.

marker, providing an average reduction in error of 70.68 %. This error might have been reduced further if the inertia of the cameras had been included in the dynamic model of the system. However, the effect of the camera's inertia was not included because in a real world application it was assumed the camera's inertia would be negligable when compared to the inertia of the wing on which it would be mounted.

## 4.4 Experiment to Represent Gust Conditions

To futher understand the concepts presented in Section 2.4 a simple demonstration was performed to show how the first bending mode of a wing is expected to dominate the flexible

response of an aircraft in turbulence. Using the experimental setup outlined in this chapter, random noise from 0 - 200 Hz was input to the shaker, and the response at the beam tip was measured for 100 averages. Figure 4.9 shows the random noise input (top) and the beam response (bottom), and Figure 4.10 shows the results in the frequency domain with a clear indication that the first mode is dominant. The coherence plot shown above the frequency response is used to quantify the signal quality which in this case is on the lower end of acceptible coherence values at around 76 %. However, this demonstration of dominant first mode behavior allows for a single frequency, the frequency of the first mode, to be tracked in order to determine points at which images can be collected. This technique will be used latter on in this paper.

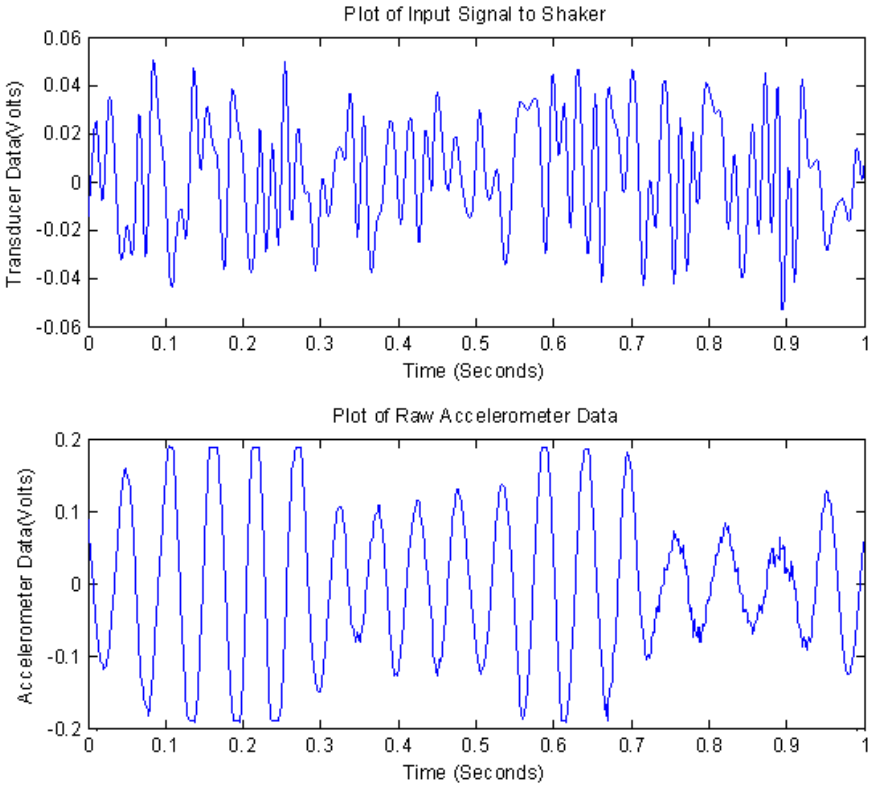


Figure 4.9: Input to Shaker (Top).Raw Data from Accelerometer (Bottom).

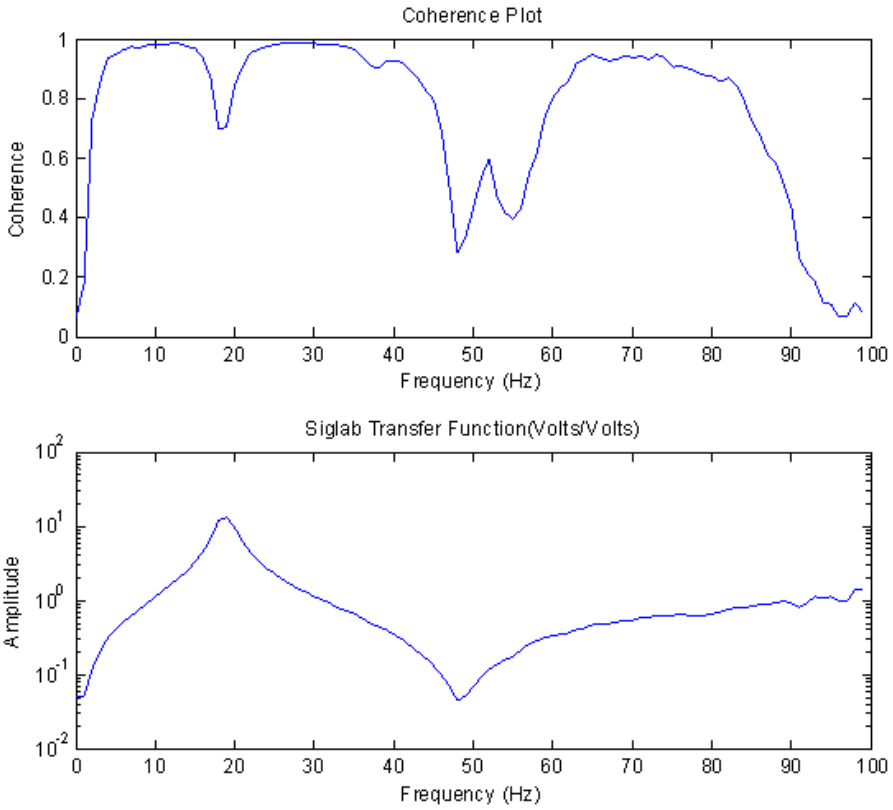


Figure 4.10: Coherence Plot (Top). Transfer Function (Bottom).

# Chapter 5

# Dynamic Model of an Unmanned Aircraft

## 5.1 Ground Vibration Testing

Ground vibration testing (GVT) is used to obtain experimental data that will enable the validation and improvement of dynamic models of the structure tested. One of the main objectives of ground vibration testing for aircraft is to obtain modes of vibration for flutter prediction. In this case, a modal test characterizes the dynamic response of the structure so that appropriate corrections can be applied.


Figure 5.1: Shaker excitation of aircraft engine[6].

### 5.1.1 Use of Finite Element Analysis in GVT

One method that aids in reducing the cost of GVT is the use of finite element analysis (FEA). With the aid of programs such as Abacus, Ansys, Nastran, or other software solutions, it is possible to simulate full vehicle modes before a test of the actual structure. Figure 5.2 gives an example of such a finite element model of an arbitrary wing panel. In this particular example, the results of FEA analysis were used to predict the mode shapes of a wing panel.

While finite element models can usually provide estimates of the dynamic behavior of aerial vehicles, it is imperative that a modal test of the aircraft be performed to validate such a model. Coupling the information gained from FEA software and analytical models, modal pretest procedures are formed around the operating conditions of the aircraft to be tested.

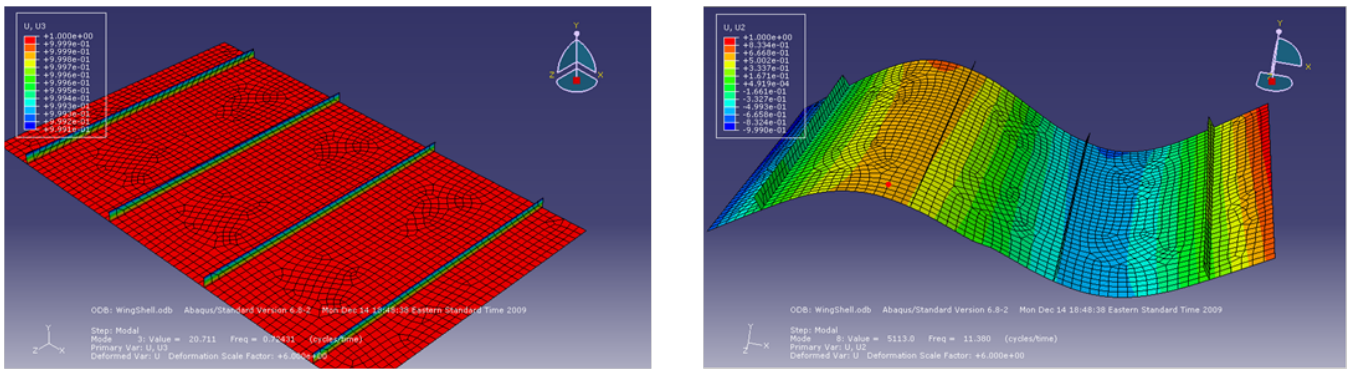

Figure 5.2: FEA model of wing panel(right).Second bending mode estimate using FEA (Left).

Modal pretesting, which is outlined in [6], gives the engineer several guidelines for ensuring that the most efficient test procedures are carried out when analyzing aircraft structures. Proper understanding of topics such as practical frequency ranges to test over, the number of degrees of freedom to be tested, the location of inputs, and the number of outputs can all have great influence on the tests that are to be executed.

### 5.1.2 Boundary Condition Considerations

Designing a modal test which produces the desired structural responses representative of in-flight conditions are essential to achieve logical results. To achieve these realistic responses, careful consideration must be given to the vehicle boundary conditions. Formulation of the proper boundary conditions in a modal test will not only provide results representative of in flight conditions, but it will also allow for unconstrained motion of the unmanned vehicle in question and prevent external vibrations from producing false modes that would not be present in normal operations [4],[10].

The creation of the free-free conditions needed to test larger aircraft involves arranging the aircraft in a manner that is similar to a test flight configuration. This means setting all control services to 0°of deflection, leaving all hydraulic and control systems active and serviceable, and flattening the tires on landing gear to create ideal testing conditions. However, for the much smaller unmanned aircraft that will be used in this research, we will use an alternate method Whoehrle refers to as the bungee cord method. By suspending the flying wing with bungee cord or a flexible equivalent, it is possible to mimic the free-free boundary conditions seen by our test vehicle in flight.

### 5.1.3 GVT Testing Techniques

Results of GVT are obtained by using shakers to excite the aircraft structure and measure its response in the form of a frequency response function (FRF) through the use of accelerometers and force transducers as shown in figure 5.1. The shakers used in these experiments excite the structure using random burst or harmonic swept-sine excitation. Each signal type will vary in the amount of spectral energy that it contains and the test duration needed for information gathering. However, Peeters [6] combines several signals in a method to identify critical modes and visualize their shapes. Table 5.1.3 summarizes the test strategy used to evaluate aircraft used in Peeters evaluation.

Typically, the first test that is to be carried out is a random excitation of the aircraft structure. This test, called a survey, will give the experimenter a good first indication of

Table 5.1: Summary of Modal Testing Operations

| Modal Test | Result Achieved from Test |
|---|---|
| Random Burst | First indication of system resonances |
| Swept-Sine | Higher quality FRF in the frequency range of interest |
| Sine-Dwell(Normal Mode Testing) | Investigion of individual modes found in swept-sine test |

any resonances that may be present. However, due to the low energy input at low frequency ranges, FRF's are usually poor at the driving points. It is for this reason that the a swept-sine or stepped sine test is performed. In more recent testing of larger aircraft, swept-sine tests have become more common since they require less time. Another advantage of this test is a higher quality frequency response function. After evaluation of the FRF achieved from a swept-sine test, normal mode testing is performed in order to identify and visualize critical modes of interest.

## 5.2 Experimental Setup

To test whether or not the method of stereo image correction explained in Lanier and Short [18] holds true in flight conditions, a second test will be conducted using an experimental flying wing. This vehicle was designed for use as an autonomous surveillence platform and will serve as an initial test platform for this research. Performing a modal examination of this wing will require that the wing be suspended in a manner that will allow the structure to respond in a fashion that will be representative of actual flight conditions. For this response to happen the wing will be suspended using a technique that Woehrle [10] refers to as the

bungee cord method.

A wooden frame made of 2" X 4" planks was constructed to provide a structure that will support the flying wing. Then, using 1/8 " bungee cord, the wing is suspended by three points on the vehicle, two of which are the mounting hooks on the wings and the third is a eye screw placed on the motor mount. Suspending the wing in this fashion, which is shown in figure 5.3, will allow for a response that should resemble the vehicle's natural flight behavior.

Figure 5.3: Experimental flying wing suspended from wooden frame with bungee cords.

After suspending the wing on our wooden frame, accelerometers will be placed in two rows along the wing spaced 8 inches apart. This spacing, demonstrated in figure 5.4, is measured from the center line of the wing. Each row will be parallel to either the leading edge or trailing edge of the wing and will be placed three inches inside this edge. This

accelerometer placement will make it possible to map the mode shape of the wing by plotting the magnitudes of the imaginary accelerance values found at each modal frequency.

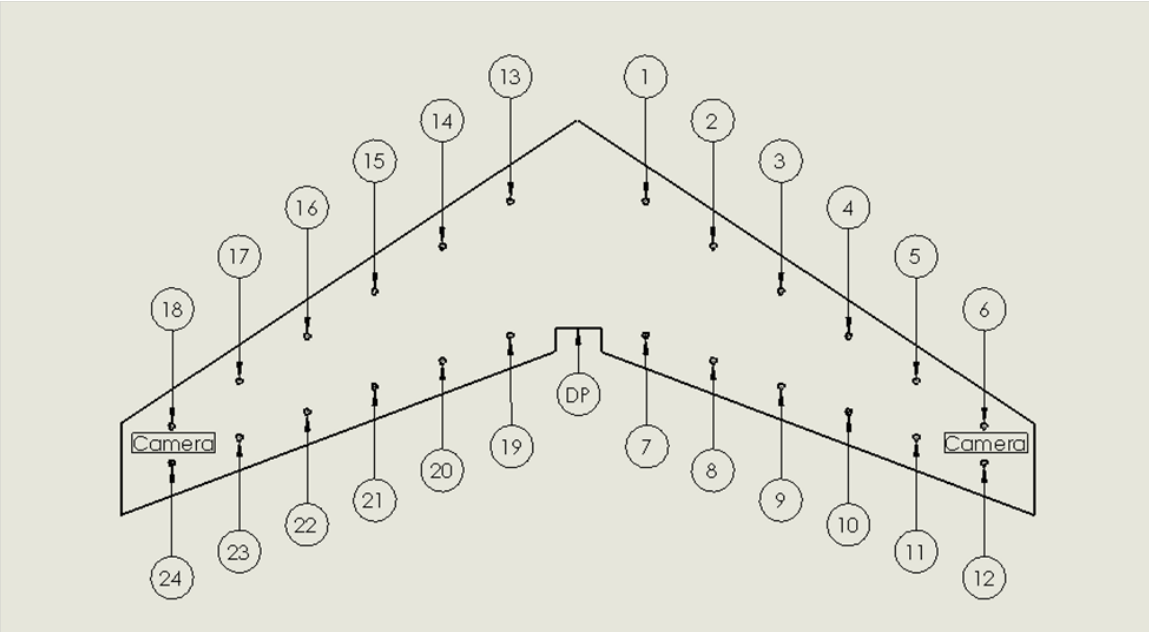


Figure 5.4: Outline of experimental flying wing accelerometer placement.The driving point measurement is represented by the "DP" callout.

The digital signal analyzer, a four channel Siglab 2024 DSP unit, will be used to collect data from the 24 points selected along the wing with PCB model 35C65 accels. These accels will be attached to the flat bottom of the experimental wing with wax. Since the placement of these accelerometers will have the effect of mass loading the wing and all twelve measurements will not be taken at one time due to the channel limitations of the Siglab unit, dummy masses will be employed to represent the mass loading of the accelerometers in the locations where measurements are set to be taken but which are not currently being measured.

Using the firewall of the experimental wing, a force transducer, PCB model Y208C02,was attached using super glue. Excitation of the wing will take place at this point,which is also

Figure 5.5: Close-up showing accelerometer and dummy mass placement.

the wing's center of gravity, and a driving point FRF will be collected here. A 2 lb-f Ling Dynamics Shaker, model V203, will be used to provide the frequency input to the wing. A 10-32 threaded nylon rod will serve as stinger connection between the shaker and the force transducer in an effort to ensure the wing is excited in only one direction [4].

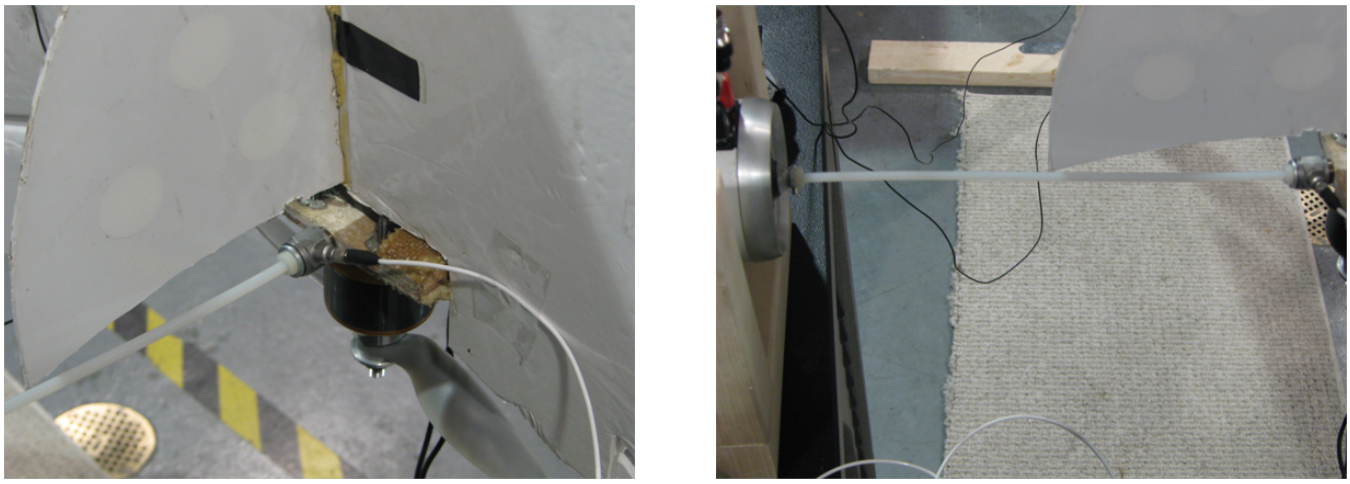

Figure 5.6: Force Transducer (PCB model Y208C02) attachment to wing firewall(Left). Threaded 10-32 nylon rod is used as a stinger between the shaker and force transducer(Right).

# Chapter 6

# Experimental Results of a Stereo Camera System Installed on a UAV

Upon completion of the experimental setup, random burst excitation was used to perform and initial survey of the experimental flying wing. This signal is composed of random noise with a bandwidth of 0-100 Hz at an RMS amplitude of 0.015 volts. The duration of the excitation was one second with a rest period of four seconds. This excitation was repeated twenty times and then averaged. The first point of measurement for the structural response of the flying wing will be the driving point at the firewall of the wing since it will provide the cleanest frequency response function. Figure 6.1 is an example plot of the response signals seen at the force transducer and accelerometer placed at the driving point.

After measuring the structural response at the driving point, 24 separate frequency

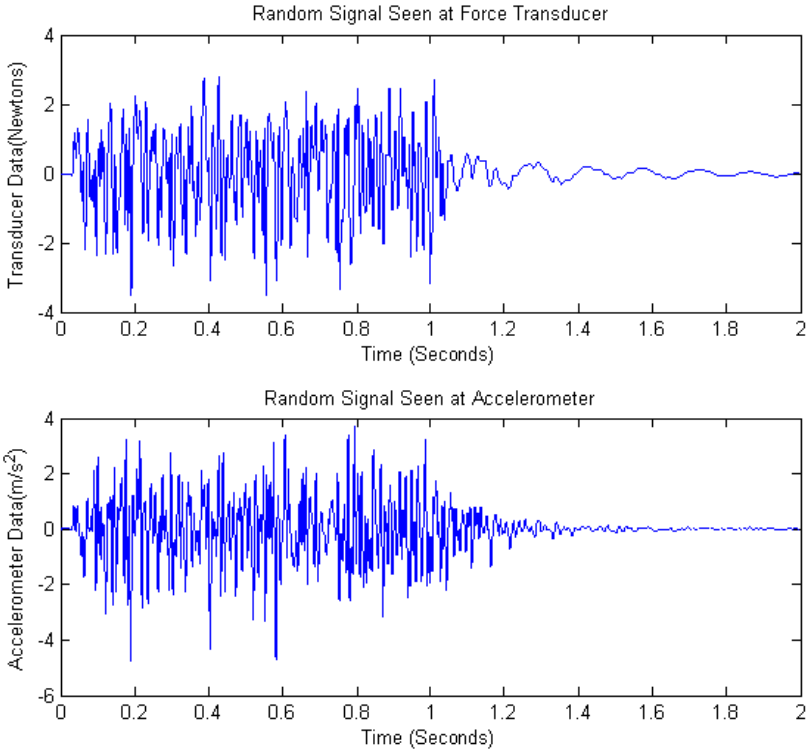


Figure 6.1: Random signal measured at the force transducer(Top).Random signal measured at accelerometer(Right).

response functions will be collected, over the same number of averages as the driving point response, at designated points across the wing identified in the experiemental setup. The measurements collected at these points will be used to visualize the dominate mode shape of the flying wing. It is from this mode shape that the deflection and slope of each wing tip camera will be determined.

## 6.1 Driving Point Frequency Response

Transformation of the information shown in figure 6.1 into the frequency domain will yield the frequency response function (FRF) of the experimental wing. Shown in figure 6.2, it is clear that the first flexible mode of the experimental wing is present at a frequency of 15.5 Hz as indicated by the phase shift shown in the same figure. Two latter peaks are identified at 36 Hz and 41 Hz. Since their amplitudes are approximately an order of magnitude lower that the amplitude of the first natural frequency, their contributions to the mode shape of the wing will be almost negligible. The quality of the FRF is evaluated using the coherence function. Figure 6.3 clearly the shows the coherence level at 15.5 Hz to be 99.9%well above the minimum acceptible threshold of 75 %.

### 6.1.1 Linearity Test for Flying Wing

For the modal analysis performed in this research, it is assumed that the response of the structure under examination is a linear function of the force used to excite it. To test the structural linearity of the flying wing used in this experiment, several additional surveys were taken at the driving point. Using a range of amplitudes from 0.005 volts RMS to 0.030 volts RMS to excite the wing, and the magnitudes of the first modal peaks were plotted to examine the assumption of linearity. This plot is shown in figure 6.4.

Examination of lower excitation levels when compared to the the level of 0.015 volts rms that was used in the initial modal survey show there is a 30 %increase in the magnitude

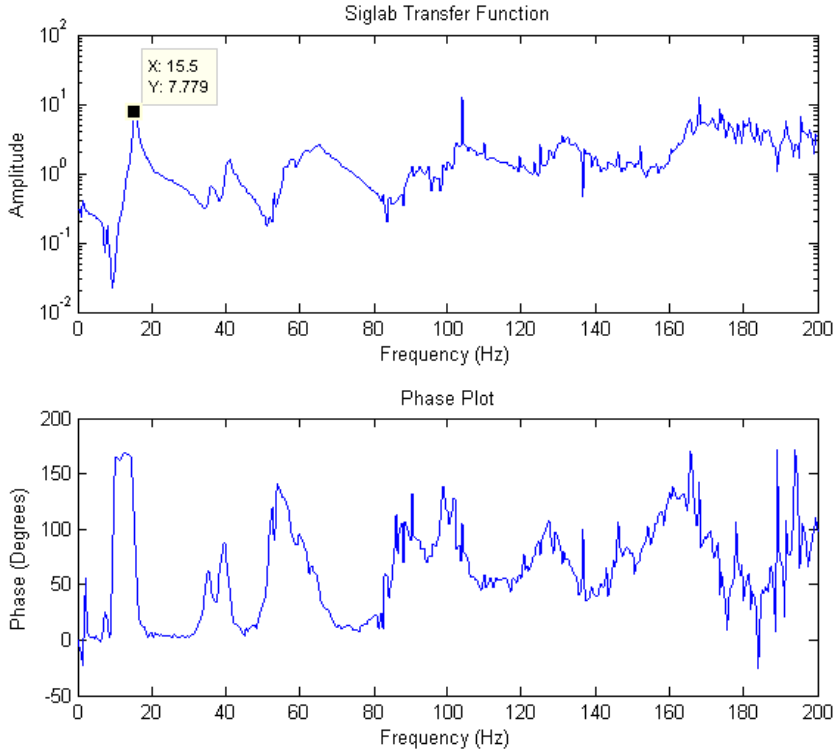


Figure 6.2: Frequency Response Function of Flying wing, the first mode of the wing is shown at 15.5 Hz(Top).Phase plot shown positively identifies first mode by showing 180 degree phase shift at 15.5 Hz(Bottom).

of the first modal peak when the amplitude is decreased by approximately 70 %. It must be noted however, that the coherence of the data gathered in this lower magnitude was below 70 %making excitiations at this level undesirable for further experimentation. Further examination shows that when using higher levels of excitation, with coherence levels above 75 %, the change in the magnitude of the first modal peak is almost negligible as it settles around a constant value.

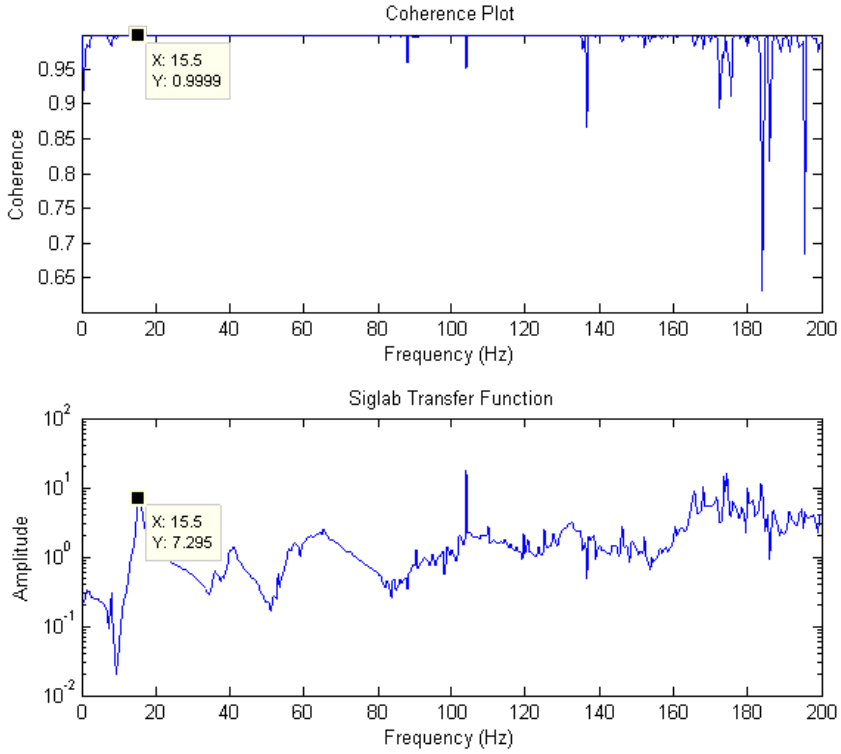


Figure 6.3: Coherence Plot of flying wing and coherence at 15.5 Hz(Top).Frequency Response Function of Flying wing(Bottom).

## 6.2 Modal Survey of Flying Wing

After collection of the driving point data, random excitation was used to collect information from each of the 24 points selected across the wing. By plotting the imaginary receptance values of each first mode frequency response gathered along the wing, it is possible to visualize the flying wing's mode shape. Note that this technique, refered to by Ewins as the peak-picking method [4], is acceptable because of the well separated mode of the flying wing. Furthermore, since this thesis focuses on the first mode of the flying wing, the 24 receptance values that are gathered will provide sufficent resolution to visualize the wing's modal de-

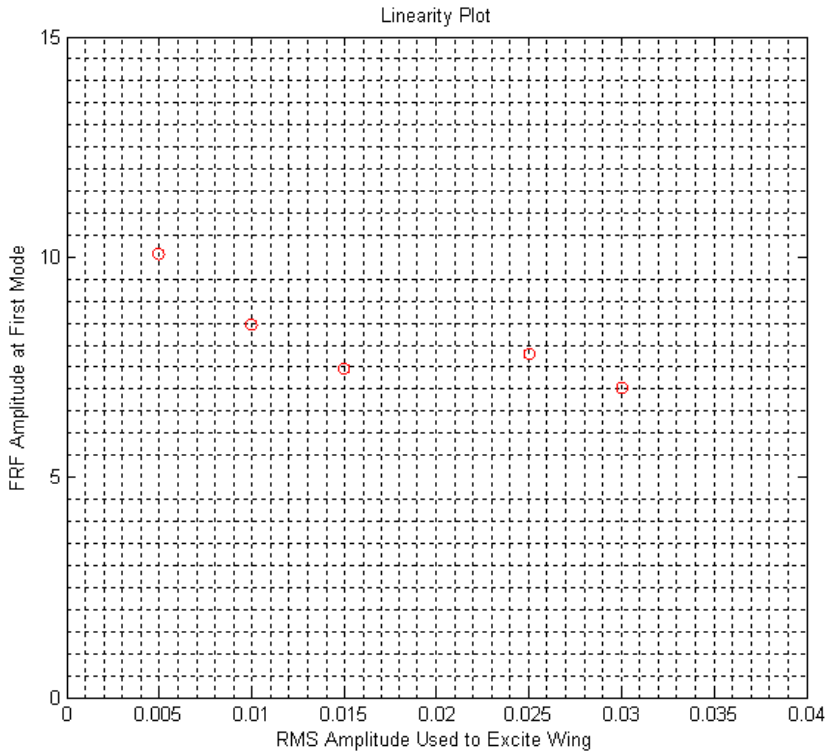


Figure 6.4: Plot of first mode magnitudes with increasing excitation magnitude.

flections according to the guidlines set mentioned by Pickrel [9]. Figure 6.5 is a snapshot of the first bending mode of the flying wing.

The snapshots shown in figure 6.5 gives a basic understanding of the structural behavior of the wing. Observation of this figure gives positive evidence of the wing's structural behavior being dominated by bending in its first mode.

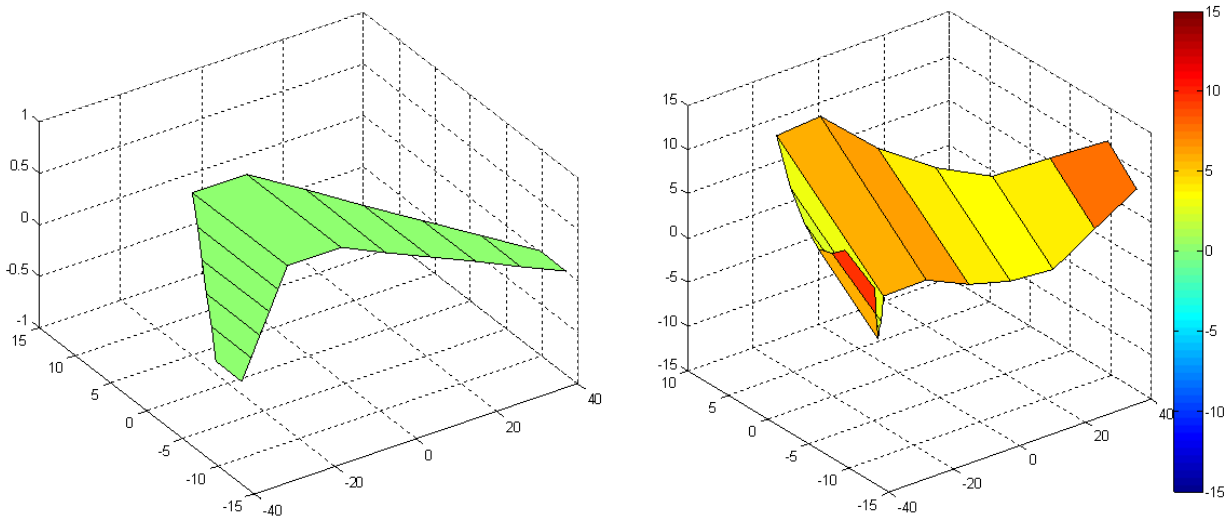


Figure 6.5: Matlab representation of the flying wing divided by points of accelerometer placement (Left). Matlab representation of the first mode shape of the flying wing (Right).

### 6.2.1 Polynomial fit of Mode Shape

While a sufficient approximation of the wing's mode shape may be achieved by plotting 24 values along the wing, it was decided that this would be an insufficent method for determining the slope of the deflected wing. Minimal guidelines state that at least 10 measurement points should be used when defining the slope or curvature of a structure [9], and even though this criterion has been met, the use of a curve-fitting method is preferred to reduce the effect of random errors that may occur in measured responses. Furthermore, by defining the slope of the flying wing as a continous equation, the correction of stereo camera angles will be made easier in the event that it becomes desirable to change the camera position along the wing span. Figure 6.6 shows the polynomial fit of the measured receptance values along the top and bottom of the wing. For each polynomial fit, a $6^{th}$-order equation was found to be the

best fit for the behavior of the wing.

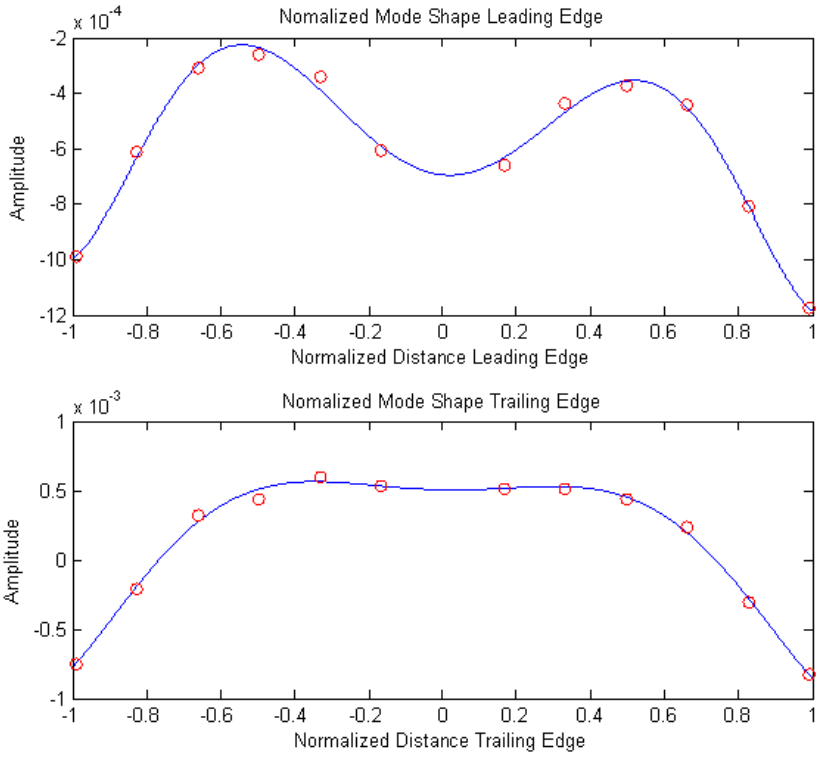


Figure 6.6: Polynomial fit of modal peaks across flying wing. Leading edge polynomial fit (top). Trailing edge polynomial fit (bottom).

Examination of figure 6.6 once again demonstrates that bending dominates the first mode behavior of this wing. However, since the cameras used in this stereo vision system are centered between the accelerometers on the leading and trailing edges of the wing, the polynomial fit of either the leading or trailing edge alone is not sufficent enough to describe camera behavior since there are slight variations in the wing's behavior in each fit. To best determine this wing's behavior, from which a camera slope will be derived, it was decided that an average of the accelerometer receptance values taken along the leading and trailing edges would be calculated and another polynomial fit would be performed. Using a polyfit of the

average receptance values will provide a better approximation of wing behavior by reducing the rounding errors that could be encountered by averaging the two $6^{th}$ order polynomials found at the leading and trailing edges. Figure 6.7 pictures this second polynomial fit.

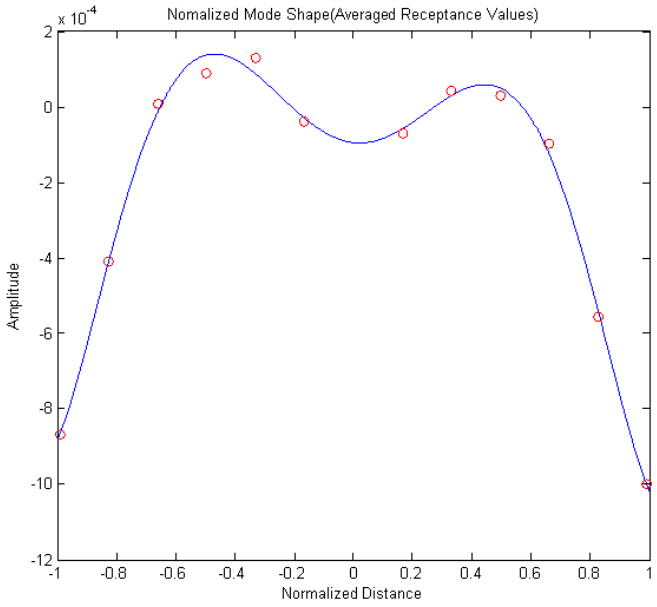


Figure 6.7: Polynomial fit of averaged modal peaks of leading and trailing edges.

### 6.2.2 Derivation of Camera Slope

After achieving a polynomial fit which is representative of the mode shape of the flying wing, the polynomial equation can then be used to approximate the camera slope as a function of their placement on the wing. This is accomplished by the use of two simple operations, the first of which is scaling the approximate mode shape to the proper deflections at the point of camera placement(maximum displacement in this case), and the latter of which involves taking the derivative of this scaled mode shape and calculating the values that also

correspond to the point of camera placement. Using this method, the slope of the left and right cameras, as they are rotating away from each other, was found to be -0.001217 radians and 0.001195 radians, respectively. The results of these operations can be seen in figure 6.8.

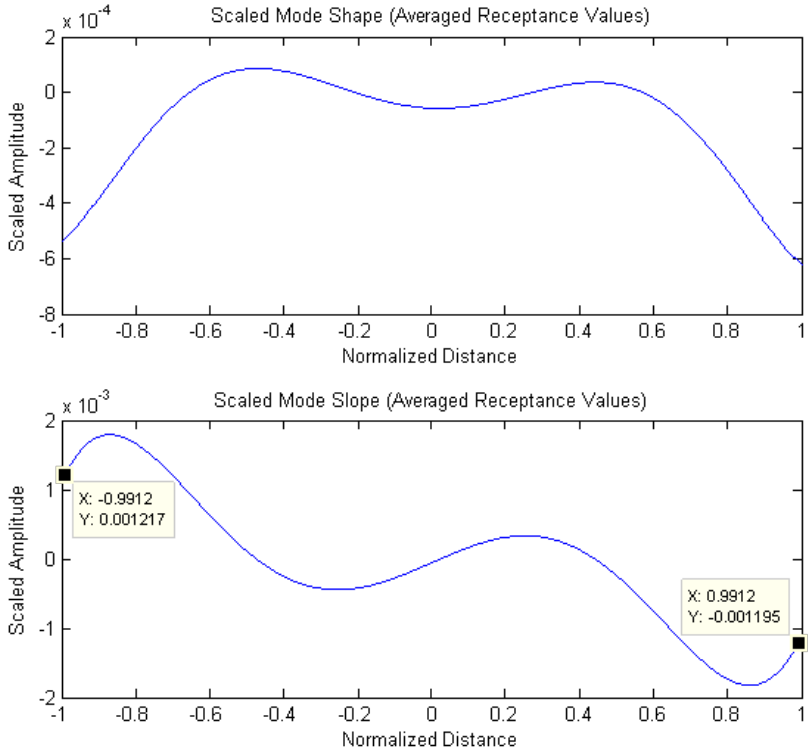


Figure 6.8: Mode shape that has been scaled to proper camera deflections(top). Slope of first experimental wing's first bending mode used to determine camera angle (bottom).

## 6.3 Results of Camera Corrections

Now that the slope of the stereo cameras has been determined at maximum deflection, utilization of the stereo image rectification method described in section 3.3 is now needed to correct distance inaccuracies. Two tests were undertaken to validate this correction method.

The first test involves correcting the images taken from the flying wing while it was excited at its first natural frequency. The second test involves correction of images taken from a flying wing using random excitation to simulate flight turbulence excitation.

### 6.3.1 Corrections Using Resonance Test

Addition of the slopes found in the previous section yield a $\Theta_y$ value of 0.002412 radians to be used in the composite rotation vector. Table 6.1 compares the stereo distance measurement values of the installed stereo system at rest to the stereo distance values found when the system is excited at resonance and no correction angle is used. Table 6.2 compares the resting stereo distance values to the values of a system excited at resonance whose images have been corrected. Comparison of these two tables reveals around an 80 %drop in distance error when using a correction angle.

Table 6.1: Error in Distance Measurement Without Camera Corrections.

| Object | Stereo Distance Measurement Without Vibration | Stereo Distance Measurement With Vibration and Without Correction Angle | Percent Error |
|---|---|---|---|
| Checker Board | 5.137 m | 5.078 m | 1.14 % |
| Bucket | 4.096 m | 4.051 m | 1.09 % |
| Cone | 3.936 m | 3.891 m | 1.14 % |

This reduction in error, however, does not translate into a significant distance reduction in this experiment because of the flying wing's large baseline, which Short [2] mentions is more suitable for long range stereo imaging. Therefore, scaling these corrections to a distance of around 60 meters will give a more realistic expectation for this process. These

Table 6.2: Error in Distance Measurement With Camera Corrections.

| Object | Stereo Distance Measurement Without Vibration | Stereo Distance Measurement With Vibration and With Correction Angle | Percent Error |
|---|---|---|---|
| Checker Board | 5.137 m | 5.148 m | .20 % |
| Bucket | 4.096 m | 4.088 m | .19 % |
| Cone | 3.936 m | 3.936 m | 0 % |

results,pictured in table 6.3, show a 55 %reduction in distance error which translates into an altitude estimation that is closer to the true distance.

Table 6.3: Scaled Stereo Vision Distance Measurement Error .

| Object | Stereo Distance Measurement Without Vibration | Stereo Distance Measurement With Vibration and Without Correction Angle | Percent Error |
|---|---|---|---|
| Object | 60 m | 52.8 m | 12 % |
| | Stereo Distance Measurement Without Vibration | Stereo Distance Measurement With Vibration and With Correction Angle | Percent Error |
| Object | 60 m | 63.4 m | 5.6 % |

### 6.3.2 Achieving Stereo Camera Corrections in the Presence of Random Excitation

The method of stereo image correction used for a stereo vision system subjected to random vibration varies slightly from that of resonance excitation and a brief explanation will be used to clarify this technique. If one were to look at the flying wing and try to make an analytical model of this system, one might break it up into a free-free lumped mass system like the one pictured in figure 6.9. From this system we would be able to determine the first

five mode shapes of the system; however, from examination of figure 6.2 it is clear that this structure's response will be dominated by first mode behavior.

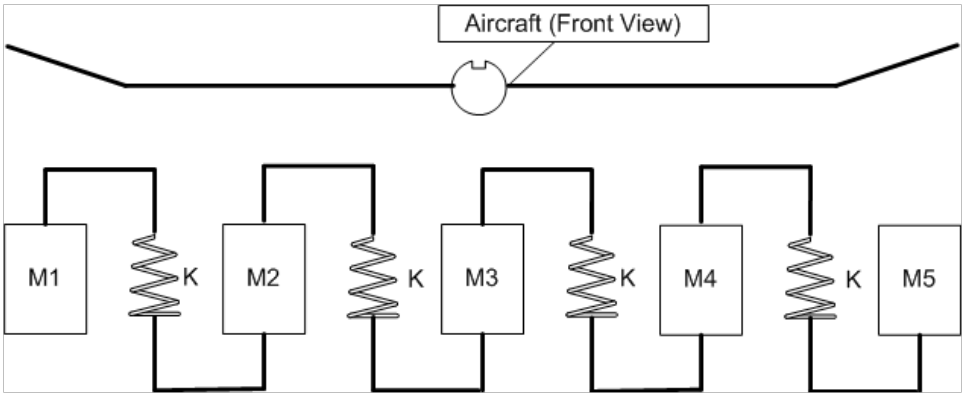


Figure 6.9: Flying wing used can be approximated as a free-free lumped mass system.

With this behavior in mind, a less complex model of the flying wing could be made to resemble figure 6.10, a system composed of a fuselage mass and two wings each possessing an equivalent mass and stiffness. This system, once solved, will yield the characteristics of the flying wing's first mode behavior necessary to find the angle needed for image correction with much less effort. However, by taking advantage of the symmetry in figure 6.10, further simplification can be achieved leaving an unrestrained two-degree of freedom system composed of a fuselage mass and an equivalent wing mass and stiffness, which is also shown in figure 6.10.

This system, pictured in figure 6.10, has a response which can be defined by equation 6.1 if we assume the masses of the system are equal. For the sake of simplicity, then, the mass of the fuselage and the mass of the wings are assumed to be equivalent. This expression breaks the system response into two distinct mode shapes that will contribute proportionally

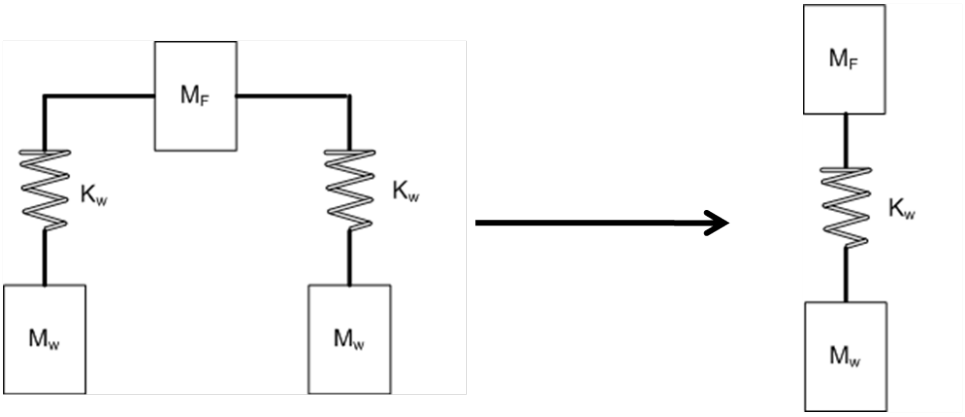


Figure 6.10: Lumped mass system simplified to a fuselage mass and two wing masses.

to the flying wing's response according to the frequency at which the system is excited. The first term can be described as the rigid body motion of the system, representation of the static wing deflection in steady unaccelerated flight. The second term can be described as the first flexible mode of the flying wing. Excitation in the range of the $1^{st}$ flexible frequency will exhibit a response that is the summation of the rigid body (static deflection) and $1^{st}$ bending mode of the aircraft.

$$\frac{\ddot{x}}{F} = \sum_{r=1}^{n} \left( \frac{\phi_{1r}\phi_{1r}}{-\omega^2 m_r + k_r} \right) = \frac{1}{-\omega^2 2M + 0} + \frac{1}{-\omega^2 2M + 4K_w} \tag{6.1}$$

In the modal configuration used for this thesis, the rigid body motion of the flying wing was most nearly eliminated in order to examine the flexible modes of the flying wing and the stereo camera corrections were applied accordingly. However, in actual flight conditions, will be necessary to include the effects of rigid body motion to achieve proper stereo camera correction of an aircraft in operation. The rigid body motion corresponds to mean load

factors that result in higher or lower wing loading and produce a corresponding static wing deflection. Additionally, excitation of an aircraft at resonance, similar to that of the previous experiment, will almost never happen since the gust excitation that an aircraft will experience will be random. For this reason, it is necessary to demonstrate stereo image rectification using an aircraft subjected to random excitation.

Instead of correcting images collected at a specified interval that coincides with the resonance of the flying wing, images used for stereo image rectification will now be taken using a least squares fit of the accelerometer input. This algorithm, described by Short[2], will track accelerometer inputs that correspond to $1^{st}$ mode displacement based on the phase angle and dominant frequency of the signal. For the flying wing this dominant frequency is assumed to be first bending mode of the wing. Once a point for an image capture is selected, the acceleration is recorded and converted to a receptance value that can be used to scale the polyfitted mode shape and achieve the proper correction angle.

### 6.3.3 Results of Stereo Camera Corrections in the Presence of Random Excitation

To simulate in-flight turbulence, the flying wing aircraft was excited using a continuous random signal at 0.030 volt rms with frequencies from 0-50 Hz as continous images were taken. Using the method described in the previous section, image collection points were selected and their acceleration values were recorded and used to determine the proper camera

angle. A graph of the accelerometer response is shown in figure 6.11. Repeating the procedure found in section 6.2.2 the angle at maximum deflection was found to be 0.002469 radians. The result of applying this correction angle to the images is shown in table 6.4.

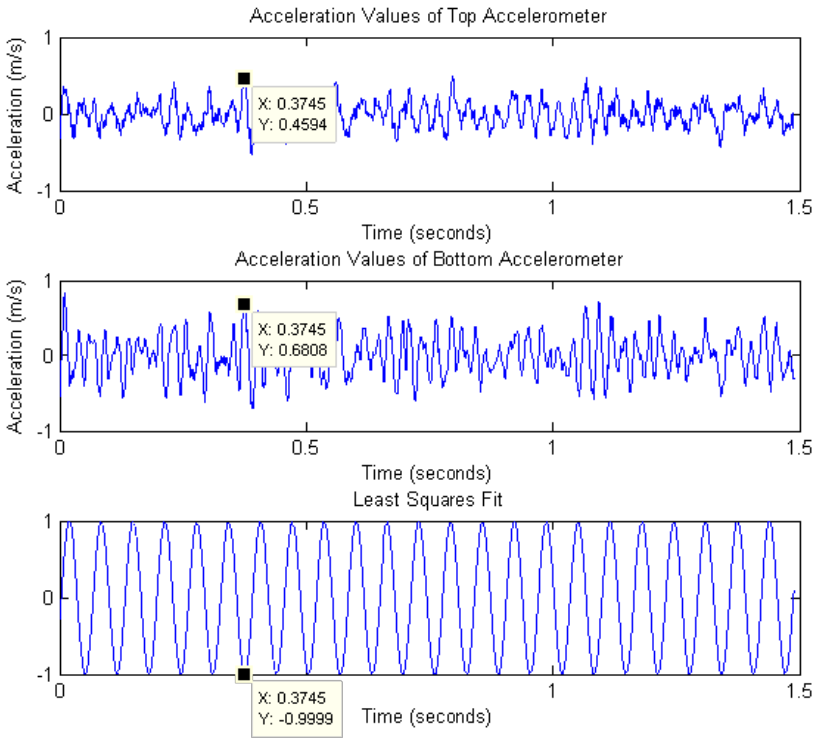


Figure 6.11: Acclerometer response of top wing tip camera accel(top). Accelerometer response of bottom wing tip accel(middle). Point of image capture determined by least squares fit(bottom).

Once again applying the camera's deflection angle to the Rodriugez rotation matrix results in a error reduction of over 70 %. However, it must again be noted that the large baseline of this stereo vision system doesn't allow for a significant distance reduction since the object in focus is placed at a distance of just over 5 meters, so this measurement must once again be scaled in order to understand the true benefit of this technique. Table 6.5

Table 6.4: Stereo Vision Distance Measurement Error in Random Excitation.

| Object | Stereo Distance Measurement Without Vibration | Stereo Distance Measurement With Vibration and Without Correction Angle | Percent Error |
|---|---|---|---|
| Object | 5.137 m | 5.04 m | 1.89 % |
| | Stereo Distance Measurement Without Vibration | Stereo Distance Measurement With Vibration and With Correction Angle | Percent Error |
| Object | 5.137 m | 5.114 m | .45 % |

shows the results once again scaled to a distance of 60 meter where it is possible to see that a 71.4 %error reduction places the stereo distance estimate 7.61 meters closer to the actual distance.

Table 6.5: Stereo Vision Distance Measurement Error in Random Excitation.

| Object | Stereo Distance Measurement Without Vibration | Stereo Distance Measurement With Vibration and Without Correction Angle | Percent Error |
|---|---|---|---|
| Object | 60 m | 49.36 m | 17.7 % |
| | Stereo Distance Measurement Without Vibration | Stereo Distance Measurement With Vibration and With Correction Angle | Percent Error |
| Object | 60 m | 56.97 m | 5.05 % |

These results indicate that a stereo system mounted to the wingtips of an aircraft will be capable of extracting accurate distance information once the modal characteristics are defined. Large-baseline stereo imagery has applications in high-altitude aerial mapping that are greatly enhanced with this system. To accurately measure camera deflections in-situ, an accelerometer mounted to the fuselage and accels mounted to the wingtips should provide the necessary degrees of freedom for shape extraction.

# Chapter 7

# Conclusions and Recommendations

This thesis presents work and research performed to develop a method to correct large baseline stereo distance measurements in vibration environments. The following sections are a summary of the work completed as well as some suggestions for future work that may improve upon this research.

## 7.1 Summary of Work

A dynamic model of a flexible stereo vision system was created to estimate its expected behavior. The behaviors of primary concern were stereo boom deflection and stereo camera angle in relation to the stereo boom deflection. An Euler-Bernoulli model of a cantilever beam was ultimately chosen to estimate camera deflection and camera slope. Construction of a flexible stereo boom system was completed to test the validity of the dynamic equations

created. Resonance excitation was used to excite the flexible stereo vision boom as stereo camera deflections were observed and used to obtain stereo camera slopes. Using a method of image rectification discussed in Lanier and Short [18], the slopes that were obtained were used to correct the images collected while the stereo beam was being excited. Stereo distance estimates of corrected and uncorrected images were compared and it was found that image corrections reduced distance errors by 70.68 %. It is believed that taking the inertia of the stereo camera into consideration may provide greater accuracy when trying to correct stereo distance. The camera's inertia, however, was not included in the dynamic model because it would most likely not be a consideration in real world conditions as its mass would be negligible in comparison the that of the wing of an unmanned aircraft.

Following this procedure, an experiment was undertaken to reproduce this reduction in error on an unmanned vehicle. An experimental flying wing was chosen as a test platform and was outfitted with a stereo vision system with a baseline in excess of five feet. This system was suspended using the bungee cord method and a modal survey was conducted using random excitation. By examining of the system's frequency response function (FRF) and using the peak-picking method, a virtual representation of the first flexible mode of the flying wing was created. Additionally, this mode shape was used to scale the modal deflections when the flying wing was excited at its first natural frequency and achieve proper camera slopes for stereo image rectification. Under excitation at resonance the corrected images showed a reduction in distance error of almost 80 %. However, this reduction in error was not representative of the true reduction in distance error since the images corrected were

collected at a distance of just over 5 meters. To gain a true indication of the reduction in distance error that would be achieved in a real world condition, the results were scaled to an altitude of 60 meters where a 55 ٪reduction in error translated into estimated stereo distances being nearly 4 meters closer to the actual altitude that without stereo image rectification.

Building on the experiments performed on the flying wing aircraft, it was now necessary to test this correction method in a simulated real world condition. This test involved the application of a camera triggering method discussed by Short [2] to collect images when and aircraft wings reach maximum displacement, a behavior that will correspond to minimum camera motion and reduce image blur. Understanding that under a gust response, the wing will exhibit a dominant first mode behavior, this method was used to obtain wing deflections under random excitation, which were in turn used to scale the first mode shape of the wing. Thus the appropriate camera slopes were found and used to correct stereo distance measurements. In this experiment, corrected images showed a reduction in distance error of over 70 ٪. This trial, also conducted at a distance of 5 meters, was scaled to an altitude of 60 meters to gain a better understanding of what the reduction in distance error would look like in real world conditions. This yielded a reduction in error of 71.4 ٪placing stereo distance measurments 7.61 meters closer to the desired result.

The system proposed can be applied to aircraft in general, where stereo cameras are mounted to the wingtips to increase baseline distance. An accelerometer mounted with the cameras and at the fuselage will provide deflection used for image correction.

## 7.2 Future Considerations

While this thesis provides some groundwork for image correction in flexible and large baseline stereo vision systems, this is not a complete system, leaving room for much improvement in this area of research. Successful testing in alternate areas could lead to the development of a complete system that may be used in military or commercial applications.

The dynamic model of the initial system used in chapter 3 was very simple in comparison the the actual behavior of a wing, but this was used as a starting point to prove that the concepts developed in this thesis have merit. Future experimentation should focus on trying to derive more complex beam behavior and investigate their effects on this stereo image correction method. Additionally, since not all wings can be assumed to behave as beams, alternate dynamic models should be explored to develop alternate applications of this correction method.

With regards to the application of stereo camera corrections applied to the flying wing aircraft, several areas could be improved. The first path would be performing an extensive finite element analysis on the aircraft to get the most accurate estimate of its behavior. This analysis would help provide the more accurate estimates of camera behavior and possibly provide greater reductions in distance error. Furthermore, if this were to be implemented as a real-world system, a full FE analysis would be performed on the aircraft before flight testing to gather information about critical modes in every section of an aircraft, and not just the wings. In addition to performing finite element analysis on the flying wing aircraft

used in this experiment it would be beneficial to analyze several other unmanned aircraft to find out whether stereo distance error also improves when this correction method is applied to different types if fixed wing aircraft.

# Bibliography


[1] B. Newhall. *Airborne camera: the world from the air and outer space*. Hasting House, 1969.

[2] Nathan Short. 3-D Point Cloud Generation from Rigid and Flexible Stereo Vision Systems. Master's thesis, Virginia Polytechnic Institute and State University, 2009.

[3] A.T. Sharkasi. Stereo Vision Based Aerial Mapping Using GPS and Inertial Sensors. Master's thesis, Virginia Polytechnic Institute and State University, 2008.

[4] DJ Ewins. Modal Testing: Theory and Practice (Letchworth, 1986.

[5] Hans-Leo Richter. Mobile vibration tests save time and money in the development of new airliners a report. http://www.dlr.de/en/desktopdefault.aspx/tabid-5105/8598_read-19056/8598_page-2/, August 2009.

[6] B. Peeters, W. Hendricx, J. Debille, and H. Climent. Modern Solutions for Ground Vibration Testing of Large Aircraft. *Sound & Vibration*, 43(1):8–15, 2009.

[7] M.W. Kehoe. Aircraft Flight Flutter Testing at the NASA Ames-Dryden Flight Research Facility. *NASA TM-100417, May*, 1988.

[8] C.R. Pickrel. Airplane Ground Vibration Testing-Nominal Modal Model Correlation. *Sound and Vibration*, 36(11):18–23, 2002.

[9] C.R. Pickrel. A practical approach to modal pretest design. *Mechanical Systems and Signal Processing*, 13:271–295, 1999.

[10] TG Woehrle, BW Costerus, and CL Lee. Modal Analysis of PATHFINDER Unmanned Air Vehicle. In *PROCEEDINGS-SPIE THE INTERNATIONAL SOCIETY FOR OPTICAL ENGINEERING*, pages 1687–1687. SPIE INTERNATIONAL SOCIETY FOR OPTICAL, 1994.

[11] W. Su. *Coupled Nonlinear Aeroelasticity and Flight Dynamics of Fully Flexible Aircraft*. PhD thesis, The University of Michigan, 2008.

[12] M. Manjuprasad. Aeroelastic random gust response analysis of aircraft structures in time domain using simulations. 2008.

[13] F.M. Hoblit. *Gust loads on aircraft: concepts and applications*. Aiaa, 1988.

[14] SHR Eslimy-Isfahany and JR Banerjee. Dynamic response of composite beams with application to aircraft wings. *Journal of aircraft*, 34(6):785–791, 1997.

[15] AV Balakrishnan. Modeling Response of Flexible High-Aspect-Ratio Wings to Wind Turbulence. *Journal of Aerospace Engineering*, 19:121, 2006.

[16] F.V. Bennett and R.T. Yntema. Evaluation of Several Approximate Methods for Calculating the Symmetrical Bending-Moment Response of Flexible Airplanes to Isotropic Atmospheric Turbulence. *NASA*, (19980230604), 1959.

[17] D.J. Inman and DJ Inman. *Engineering vibration*. Prentice Hall Upper Saddle River, New Jersey, 2001.

[18] P. Lanier, N. Short, K. Kochersberger, and L. Abbott. Modal-based Camera Correction for Large Pitch Stereo Imaging. In *Proceedings of the 24th International Modal Analysis Conference*, 2009.